โครงสร้างเฉพาะบริเวณของผลึกนาโนแมกนีเซียมซิงค์ออกไซด์

นายจารุ จุติมูสิก

LOCAL STRUCTURE OF MAGNESIUM ZINC OXIDE

NANOCRYSTALS

Jaru Jutimoosik

A Thesis Submitted in Partial Fulfillment of the Requirements for the

Degree of Master of Science in Physics

Suranaree University of Technology

Academic Year 2010

LOCAL STRUCTURE OF MAGNESIUM ZINC OXIDE

NANOCRYSTALS

Suranaree University of Technology has approved this thesis submitted in partial fulfillment of the requirements for a Master's Degree.

Thesis Examining Committee

_____

(Asst. Prof. Dr. Chinorat Kobdaj)

Chairperson

_____

(Dr. Saroj Rujirawat)

Member (Thesis Advisor)

_____

(Prof. Dr. Sukit Limpijumnong)

 Member

_____

(Assoc. Prof. Dr. Prayoon Songsiriritthigul)

Member

_____

(Asst. Prof. Dr. Rattikorn Yimnirun)

Member

_____ _____

(Prof. Dr. Sukit Limpijumnong) (Assoc. Prof. Dr. Prapun Manyum)

Vice Rector for Academic Affairs Dean of Institute of Science

จารุ จุติมูสิก : โครงสร้างเฉพาะบริเวณของผลึกนาโนแมกนีเซียมซิงค์ออกไซด์ (LOCAL STRUCTURE OF MAGNESIUM ZINC OXIDE NANOCRYSTALS) อาจารย์ที่ปรึกษา : ดร.สาโรช รุจิรวรรธน์, 114 หน้า.

แมกนีเซียมซิงค์ออกไซด์ เป็นสารประกอบกึ่งตัวนำที่มีช่องว่างแถบพลังงานกว้าง ซึ่ง สามารถปรับค่าได้ครอบคลุมในช่วง 3.3-7.8 อิเล็กตรอนโวล์ ทำให้เป็นที่นิยมในการนำมา ประยุกต์ใช้กับทัศนอุปกรณ์อิเล็กทรอนิกส์สำหรับแสงในย่านความถี่อัลตราไวโอเลต   ในทาง ทฤษฎีนั้น แมกนีเซียมซิงค์ออกไซด์สามารถเตรียมขึ้นได้จากการอัลลอยซิงค์ออกไซด์ให้เข้ากับ แมกนีเซียมออกไซด์ และเนื่องจากแมกนีเซียมออกไซด์มีโครงสร้างแบบร็อคซอลต์ ขณะที่ซิงค์ ออกไซด์มีโครงสร้างแบบเวอร์ทไซท์ ดังนั้นอัลลอยของแมกนีเซียมซิงค์ออกไซด์จึงควรจะมี โครงสร้างทั้งแบบเวอร์ทไซท์และร็อคซอลต์ ทั้งนี้ขึ้นอยู่กับอัตราส่วนของปริมาณแมกนีเซียมและ สังกะสีที่ใช้ในการเตรียม ในการศึกษาครั้งนี้ได้เสนอวิธีการตกตะกอนร่วมเพื่อใช้ในการสังเคราะห์ ผลึกนาโนแมกนีเซียมซิงค์ออกไซด์ที่มีปริมาณของแมกนีเซียมในอัตราส่วนต่าง ๆ กัน และในการ วิเคราะห์ สมบัติทางโครงสร้างของผลึกนาโนแมกนีเซียมซิงค์ออกไซด์ที่เตรียมขึ้นนั้น ได้ใช้ เครื่องมือวิเคราะห์แบบมาตรฐานต่าง ๆ ร่วมกับเทคนิคสเปกโทรสโกปีการดูดกลืนรังสีเอกซ์ ซึ่งจะ นำมาใช้ศึกษาโครงสร้างเฉพาะบริเวณของอะตอมแมกนีเซียมและสังกะสีในผลึกนาโนแมกนีเซียม ซิงค์ออกไซด์ที่เตรียมขึ้น

จากการศึกษาด้วยวิธีการเลี้ยวเบนรังสีเอกซ์ พบว่าสารตัวอย่างแมกนีเซียมซิงค์ออกไซด์ที่มี ปริมาณแมกนีเซียมน้อยกว่าหรือเท่ากับ 4% จะมีโครงสร้างเป็นแบบเวอร์ทไซท์ และสารตัวอย่าง แมกนีเซียมซิงค์ออกไซด์ที่มีปริมาณแมกนีเซียมมากกว่าหรือเท่ากับ 90% จะมีโครงสร้างเป็น แบบร็อคซอลต์ สำหรับสารตัวอย่างที่มีปริมาณแมกนีเซียมอยู่ระหว่าง 4% ถึง 90% จะมีทั้งเฟสของ เวอร์ทไซท์และร็อคซอลต์ผสมกันอยู่ ทั้งนี้ไม่ปรากฏว่ามีการเปลี่ยนโครงสร้างเฟสอย่างชัดเจน เกิดขึ้นภายใต้เงื่อนไขที่ได้ทำการสังเคราะห์ สำหรับขนาดของผลึกสารตัวอย่างนั้น พบว่ามี แนวโน้มเล็กลงเมื่อปริมาณแมกนีเซียมเพิ่มสูงขึ้น ซึ่งสอดคล้องกับการศึกษาโดยใช้กล้องจุลทรรศน์ อิเล็กตรอนแบบส่องผ่าน และ การศึกษาด้วยวิธีการเลี้ยวเบนลำอิเล็กตรอน

เมื่อทำการวิเคราะห์โครงสร้างโดยรอบของอะตอมแมกนีเซียมและสังกะสีในผลึกนาโน แมกนีเซียมซิงค์ออกไซด์ โดยใช้เทคนิคสเปกโทรสโกปีการดูดกลืนรังสีเอกซ์ในช่วง โครงสร้าง บริเวณใกล้ขอบการดูดกลืน (XANES) โดยทำการวัดที่ขอบการดูดกลืน K ของอะตอมแมกนีเซียม และสังกะสี พบว่าสเปกตรัมทั้งหมดเกิดขึ้นจากโครงสร้างพื้นฐานสองแบบ นั่นคือเมื่ออะตอม โลหะมีโครงสร้างโดยรอบเป็นแบบร็อคซอลต์ (6 ทบ) และแบบเวอร์ทไซท์ (4 ทบ) จากการ

วิเคราะห์โดยใช้ การประมาณแบบเชิงเส้น ทำให้สามารถหาค่าอัตราส่วนของร็อคซอลต์ต่อเวอร์ท
ไซท์ของสารตัวอย่างทั้งหมดได้ และจากอัตราส่วนดังกล่าวพบว่าในสารตัวอย่างที่มีปริมาณ
แมกนีเซียมต่ำ ๆ อะตอมโลหะส่วนใหญ่จะอยู่ที่ตำแหน่งของเวอร์ทไซท์ สำหรับสารตัวอย่างที่มี
ปริมาณแมกนีเซียมสูง ๆ อะตอมโลหะส่วนใหญ่มักอยู่ที่ตำแหน่งของร็อคซอลต์ นอกจากนี้ ผลที่ได้
จากการทดลองโดยใช้เทคนิคสเปกโทรสโกปีการดูดกลืนรังสีเอกซ์ยังสามารถสรุปได้ว่า สาร
ตัวอย่างแต่ละตัวนั้นอะตอมแมกนีเซียมมีอัตราส่วนร็อคซอลต์ต่อเวอร์ทไซท์สูงกว่าอะตอมสังกะสี
หรือสามารถแสดงให้เห็นได้อย่างชัดเจนโดยการทดลองว่าอะตอมแมกนีเซียมชอบที่จะอยู่ใน
ตำแหน่ง 6 ทบ ขณะที่อะตอมของสังกะสีชอบที่จะอยู่ในตำแหน่ง 4 ทบมากกว่า เมื่ออัลลอยของ
แมกนีเซียมซิงค์ออกไซด์อยู่ในภาวะสมดุลทางความร้อนในระหว่างการสังเคราะห์ นอกจากนี้
อัตราส่วนของร็อคซอลต์ต่อเวอร์ทไซท์ได้ถูกนำมาใช้ในการจำลองสเปกตรัมการดูดกลืนรังสีเอกซ์
ทางทฤษฎี โดยการใช้โปรแกรม FEFF ซึ่งผลที่ได้สอดคล้องเป็นอย่างดีกับผลจากการทดลอง

สาขาวิชาฟิสิกส์ ลายมือชื่อนักศึกษา_____

ปีการศึกษา 2553 ลายมือชื่ออาจารย์ที่ปรึกษา_____

JARU JUTIMOOSIK : LOCAL STRUCTURE OF MAGNESIUM ZINC OXIDE NANOCRYSTALS. THESIS ADVISOR : SAROJ RUJIRAWAT, Ph.D. 114 PP.

MAGNESIUM ZINC OXIDE / X-RAY ABSORPTION SPECTROSCOPY/ NANOCRYSTAL

$Mg_xZn_{1-x}O$ (MZO) is an attractive wide-band gap semiconductor for deep ultraviolet optoelectronic device since its bandgap is tunable over a broad range, from 3.3-7.8 eV. In principle, MZO can be obtained from alloying MgO with ZnO. However, since MgO has rocksalt (RS) structure and ZnO has wurtzite (WZ) structure, MZO alloys would have RS and WZ structure depending on the magnesium concentration. In this study, the co-precipitation method was used to synthesize MZO nanocrystals with various Mg concentrations ($0 \leq x \leq 1$). The standard analytical instruments and the synchrotron-based x-ray absorption spectroscopy (XAS) were used to investigate the structural properties of MZO nanocrystals, especially to study the local structure of Mg and Zn in MZO nanocrystals.

From x-ray diffraction, it was found that the MZO nanocrystal samples with $x \leq 0.04$ exhibit pure WZ and the MZO samples with $x \geq 0.90$ have RS structure. For $0.04 < x < 0.90$, the samples have mixed WZ and RS phases. There is no clear evidence for the composition that structural phase transition takes place. The crystallite size tended to decrease as the Mg content increased. The results agreed well with the measurements from transmission electron microscope and electron diffraction.

Both Mg and Zn *K*-edges XANES spectra of MZO nanocrystal samples were taken to shed light on the local structure around Mg and Zn atoms. It was found that all spectra can be fitted by using two basis types when the central metal atoms resides in either RS local structure (6-folds) or WZ local structure (4-folds). By linear combination analysis the RS/WZ ratios were obtained for all samples. From RS/WZ, it was found that the majority of metal atoms occupy WZ sites for samples with low *x* and RS sites for samples with high *x*. Moreover, form XAS results, it can be concluded that for each sample (at the same concentration) Mg atom has higher RS/WZ ratio compared to that of Zn atom. This can be viewed as an experimental evidence that, in MZO alloys at thermal equilibrium, Mg atom prefers 6-fold site while Zn atom prefers 4-fold site. The RS/WZ ratios were also used for the simulation of XAS spectra using FEFF software. All features in the XANES spectra can be theoretical reproduced well in both Mg and Zn edges.

School of Physics   Student's Signature_____

Academic Year 2010   Advisor's Signature_____

ACKNOWLEDGEMENTS

Jaru Jutimoosik

CONTENTS

CONTENTS (Continued)

CONTENTS (Continued)

LIST OF TABLES

LIST OF FIGURES

LIST OF FIGURES (Continued)

LIST OF FIGURES (Continued)

LIST OF FIGURES (Continued)

LIST OF ABBREVIATIONS

CCD	=	Charge Coupled Device
CL	=	Cathodoluminescence
CRT	=	Cathode Ray Tube
EB	=	Electron Beam Evaporation
ED	=	Electron Diffraction
EDS	=	Energy Dispersive Spectroscopy
EXAFS	=	Extended X-ray Absorption Fine Structure
FEFF	=	Effective Scattering Amplitude
FMS	=	Full-Multiple Scattering
FWHM	=	Full Width at Half Maximum
IR	=	Infrared Spectroscopy
KMITL	=	King Mongkult's Institute of Technology Ladkrabang
MBE	=	Molecular Beam Epitaxy
MOVPE	=	Metalorganic Vapour Phase Epitaxy
MZO	=	$Mg_xZn_{1-x}O$
NA	=	Numerical Aperture
NMR	=	Nuclear Magnetic Resonance
PLD	=	Pulsed Laser Deposition
RF	=	Radio Frequency
RS	=	Rocksalt

LIST OF ABBREVIATIONS (Continued)

RSMS	=	Real Space Multiple Scattering
SCF	=	Self-Consistent Field
SE	=	Secondary Electrons
SEAD	=	Selected Area Electron Diffraction
SEM	=	Scanning Electron Microscope
SLRI	=	Synchrotron light Research Institute
TEM	=	Transmission Electron Microscope
UV-VIS	=	Ultraviolet-Visible Spectroscopy
WZ	=	Wurtzite
XANES	=	X-ray Absorption Near Edge Structure
XAS	=	X-ray Absorption Spectroscopy
XES	=	X-ray Emission Spectroscopy
XNCD	=	X-ray Natural Circular Dichroism
XRD	=	X-ray Diffraction

CHAPTER I

INTRODUCTION

1.1 Background

Currently, the research on semiconductor nanostructures is one of the most active topics in physics, chemistry and materials science due to its significance in both fundamental and technological aspects. In the early day, the semiconductor researchers have focused their works on group-IV semiconductors such as silicon and germanium. Then, compounds and alloys of elements from group IV, group II-VI and group III-V were studied and utilized. Presently, these new generation semiconductors in various nano-structural forms gave rise to a wide range of useful properties with varieties of applications.

In the recent years, wide bandgap semiconductors have played a crucial role in the development of optoelectronic devices for a broad range of applications. In order to make a compound semiconductor useful for new devices, one of the important requirements is the bandgap engineering. Base on the Vegard's law (Fong, Weber, and Phillips, 1976), bandgap engineering has been practiced very successfully in the many families of compound semiconductors such as gallium indium nitride (GaInN) for blue light emitter, mercury cadmium telluride (HgCdTe) for infrared detector and gallium aluminum arsenide (GaAlAs) for laser diode and high speed transistor. The same law may also be applied to materials for next generation, spintronic devices.

Recently, magnesium zinc oxide ($Mg_xZn_{1-x}O$ or MZO) alloys has been used with a certain success in deep UV detection applications.

To perform bandgap engineering, one must find the way to form solid alloys of semiconductors with desired composition. There are several methods to grow such alloys, i.e. pulsed laser deposition (PLD), molecular beam epitaxy (MBE), metalorganic vapour-phase epitaxy (MOVPE), electron beam evaporation (EBE), RF magnetron sputtering. In general, the high-tech equipments to be used for alloying semiconductor compounds are accessible only in the well-equipped laboratories. However, there are also several economic ways to synthesis nanocrystal of semiconductor alloys, i.e. via chemical routes.

In this thesis, we have selected a chemical method called "oxalate-based co-precipitation (Ertl, Knözinger, and Weitkamp, 1999)" to synthesis MZO nanocrystals by alloying ZnO with MgO. The structural properties of MZO nanocrystal samples were then characterized.

There are many characterization techniques capable for microscopic study of compound semiconductor and non crystalline materials, i.e. x-ray diffraction (XRD), infrared spectroscopy (IR), nuclear magnetic resonance (NMR) and transmission electron microscope (TEM). However, the diffraction techniques using periodic nature of material may not be used effectively in studying the microstructure around the impurities in semiconductors materials, since the components are randomly distributed. Nonetheless, x-ray absorption spectroscopy (XAS) has been shown to be an efficient way to verify the microstructure of alloys and compound semiconductors materials (Rehr and Albers, 2000).

In this thesis, characterization techniques, available at Suranaree University of Technology (SUT) and Synchrotron Light Research Institute (Public Organization), (SLRI), were used to investigate the structural properties of the resulting products. In particular, XAS was employed as a main technique to study the local structure of MZO nanocrystals prepared by oxalate-based co-precipitation. It was found that, the results obtained are unique and may not be obtained by using other characterization techniques.

1.2   Review of literatures

1.2.1   Zinc oxide

Zinc oxide is a II-VI compound semiconductor with the chemical formula ZnO. It has a direct and wind bandgap (E_G = 3.37 eV) in the near-UV spectral region and a large free-exciton binding energy (E_b = 60 meV) at room temperature. At ambient pressure and temperature, the crystal structure of ZnO is the hexagonal wurtzite (WZ) structure, as shown in Figure 1.1. This structure is characterized by two interconnecting sublattices of Zn^{2+} and O^{2-}, such that <u>each Zn ion is surrounded by a tetrahedral of O ions</u>, and *vice-versa*.
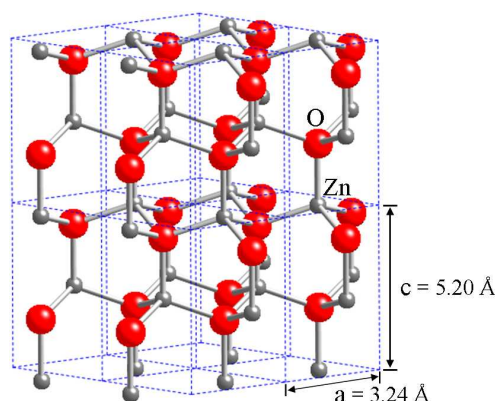
Figure 1.1 Crystal structure of ZnO (wurtzite).

ZnO is one of the potential materials for low-voltage luminescence and short wavelength light emitter (Wonga and Searson, 1999). It can be used in surface acoustic wave (SAW) devices (Hunt, 2001). In nanotechnology field, ZnO nanowire arrays hold a host of opportunities for flat screen displays, field emission sources, chemical and biological sensors, and as UV light emitters and switches (Wang, 2004). Epitaxial layers and single crystals are important for the development of optoelectronic (blue and ultraviolet light emitters and detectors), piezoelectric and spintronic devices (Norton, 2003). Epitaxial ZnO also holds much promise as a semi-conducting transparent thin film, which again will be important for solar cells, gas sensors, displays and wavelength selective applications. For mass production, zinc oxide powders have been synthesized by several techniques, such as sol-gel method (Bhattacharjec *et al*., 2002), solid-state method (Chen *et al*., 2001) and oxalate-based coprecipitation (Young-II *et al*., 2007). In general, only n-type ZnO could be consistently produced. The *p*-type doping of ZnO still be an active research topic of the present day.

1.2.2 Magnesium oxide

Magnesium oxide (MgO) is generally found in a white powdery compound. It occurs naturally as the mineral periclase or magnesia and can be prepared by thermally decomposing the mineral magnesite. The crystal structure of MgO is rocksalt (RS) structure, as show in Figure 1.2. This structure is characterized by two interconnecting sublattices of Mg^{2+} and O^{2-}, such that each Mg ion is surrounded by six O ions, and *vice-versa*.
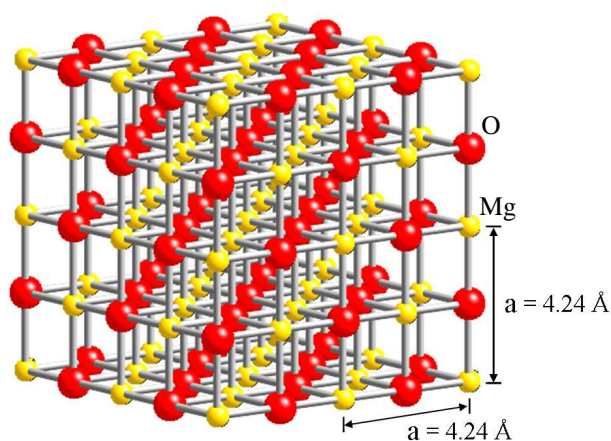
Figure 1.2 Structure of magnesium oxide (rocksalt).

Magnesium oxide can be used in various applications. For example, it is used as an insulator in industrial cables and is also one of the raw materials for making cement in dry process plants. Due to its high dielectric strength and average thermal conductivity, MgO is usually crushed and compacted with minimal airgaps or voids. Pressed MgO is used as an optical material because of it is transparent from 0.3 to 7 μm. Some properties of MgO and ZnO are compared in Table 1.1.

Table 1.1 Some properties of magnesium oxide and zinc oxide.

	Magnesium oxide	Zinc oxide
Chemical formula	MgO	ZnO
Structure	Rocksalt	Wurtzite
	a = 4.24 Å	a = 3.24 Å
		c = 5.20 Å
II-VI bond length	2.10 Å	1.98 Å
Bandgap	7.75 eV	3.37 eV

1.2.3   Bandgap engineering of MgO-ZnO

$Mg_xZn_{1-x}O$ is being considered as a candidate material for ultraviolet optoelectronic devices. According to the phase diagram of ZnO–MgO binary systems, the thermodynamic solid solubility of MgO in ZnO is normally less than 4% (Sarver, Katnack, and Hummel, 1959). However, several groups have successfully grown single phase MZO thin films with Mg content higher that 4%. Therefore, the enhancement solubility limit of MZO alloys might be explained in term of non-thermal equilibrium nature of the synthesis techniques and can be varied.

Since the crystal structures of ZnO and MgO are wurtzite and rocksalt, respectively, and the ionic radius of Zn^{2+} (0.60 Å) is quite close to Mg^{2+} (0.57 Å), alloying ZnO with the increasing concentration of Mg can lead to structural evolution from wurtzite to rocksalt and also the increase of the bandgap energy from 3.37 to 7.75 eV. However, the pathway of structural transition of WZ to RS in these material systems is still ambiguous. Based on x-ray diffraction characterization, Ohtomo and Muth (Ohtomo *et al*., 1998; Muth *et al*., 2000) reported the synthesis of single-phase $Mg_xZn_{1-x}O$ thin films with Mg concentration up to 33-36 at.% and bandgap energies up to 3.99-4.0 eV by PLD. Although there are reports of MBE (Kawasaki *et al*., 1998) and MOVPE (Park, Yi, and Jang, 2001) growths with Mg containing up to 49 at.%, most of the $Mg_xZn_{1-x}O$ thin film growth has been carried out by PLD (Sharma *et al*., 1999). It should be note that all the above-mentioned $Mg_xZn_{1-x}O$ thin films possess WZ structure.

However, continually increasing the Mg concentration, Choopun (Choopun *et al*., 2002) and Narayan (Narayan *et al*., 2002) reported the growth of RS $Mg_xZn_{1-x}O$ thin films grown by PLD, with Mg composition *x* in the range of 0.50-0.86 and 0.82-

1.00, respectively. Therefore, based on the previous works, we have summarized in Figure 3, the bandgap relations in $Mg_xZn_{1-x}O$ alloys for Mg concentration varying from 0% to 80%. It can be seen that the structure of MZO alloys reported to date can be characterized into three regimes: (1) the WZ regime (x ~0 to 0.30), (2) the RS regime (x ~0.5 to 1.0) and the mixed phase regime (x ~0.3 to 0.5). No intermediate form of MZO has been observed. It is noteworthy that in the mixed phased regime the alloys still be MZO not the phase separation of ZnO and MgO. The knowledge about local structure around Mg and Zn atoms in these alloys is important for the study of WZ/RS structural transition pathway.
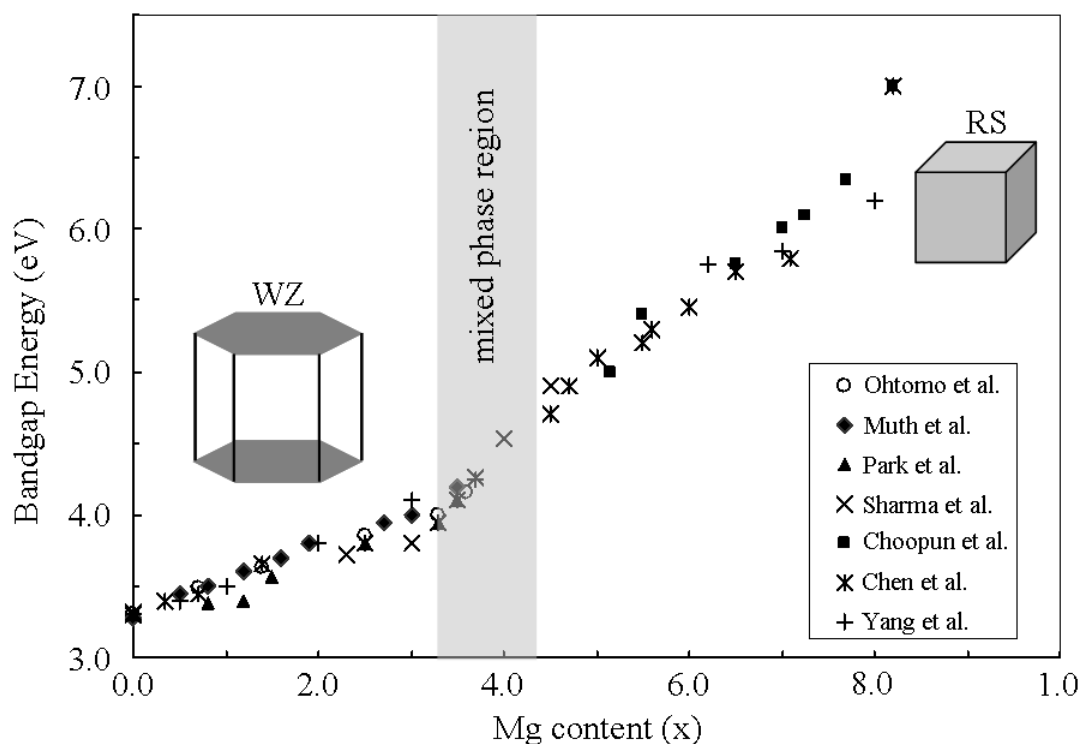
Figure 1.3 Summary of the band gap energy of $Mg_xZn_{1-x}O$ alloys as a function of Mg content.

1.2.4 Synthesis of $Mg_xZn_{1-x}O$ alloys

There are many methods to synthesis $Mg_xZn_{1-x}O$ alloys such as PLD, MBE, RF magnetron sputtering and, etc. Most of the techniques require sophisticated synthesis equipments and are not available at SUT. It is also possible to use some simple and economic way to synthesis the material. In this work, we used a process called oxalate-based co-precipitation method to explore the possibility of alloying ZnO and MgO to make nanocrystalline $Mg_xZn_{1-x}O$.

Co-precipitation method is the carrying down by a precipitate of substances normally soluble under the conditions employed. On the other hand, co-precipitation can be used to separate an element. Since the trace element is too dilute to precipitate by conventional means, it is typically coprecipitated with a carrier, a substance that has a similar crystalline structure that can incorporate the desired element.

There are three main mechanisms of co-precipitation: inclusion, adsorption and occlusion (Harvey, 2000). An inclusion occurs when the impurity occupies a lattice site in the crystal structure of the carrier and lead to a crystallographic defect. This mechanism can happen when the ionic radius and charge of the impurity are similar to those of the carrier. An adsorbate is an impurity that is weakly bound (adsorbed) to the surface of the precipitate. An occlusion occurs when an adsorbed impurity gets physically trapped inside the crystal as it grows. In this work, the starting materials which used to make $Mg_xZn_{1-x}O$ nanocrystals by oxalate-based co-precipitation method consist of zinc acetate, magnesium acetate and oxalic acid.

Lu *et al.* have experimentally studied a general polymer-based process to prepare mixed metal oxides: $Mg_xZn_{1-x}O$ nanoparticles (Lu *et al.*, 2006). The MZO nanoparticles were prepared by controlled pyrolysis of zinc/magnesium polyacrylate

complex and characterized by x-ray diffraction (XRD), transmission electron microscope (TEM), and photoluminescence (PL) spectroscopy. It was concluded that calcination of the polymer precursor at 550°C gives particles of the metastable solid solution of the ZnO/MgO system in the composition range ($x < 0.2$ and $x \geq 0.82$). The MZO particles are typically 20-50 nm in diameter. The photoluminescence in the visible is enhanced while the high-energy emission in the UV region is suppressed by incorporation of magnesium ions on zinc ion lattice sites. The $Mg_xZn_{1-x}O$ nanocrystalline start to undergo segregation into hexagonal and cubic phases upon annealing at 800°C.

In general, it is believed that alloying of ZnO and MgO proceeds by substituting Mg atoms by Zn atoms in the RS structure and *vice versa* in the WZ structure. And the different solubility limit of MgO in RS or WZ $Mg_xZn_{1-x}O$ alloys should be associated with growth mechanism as well as growth condition. XAS can be used to identify the Zn and Mg location in $Mg_xZn_{1-x}O$ alloys. Chiou *et al*. have reported that Mg-induced widening of bandgap in $Mg_xZn_{1-x}O$ nanorods revealed by x-ray emission spectroscopy (XES) and XAS (Chiou *et al*., 2008). They have found that Mg substituted at the Zn sites in the $Mg_xZn_{1-x}O$ nanorods and the structural distortion at the Zn sites increase as the Mg content increases. Park *et al*. observed a similar trend for $Mg_xZn_{1-x}O$ thin films (Park, Kim, and Seo, 2006). Recently, Maznichenko *et al*. have reported that structural phase transition and fundamental band gap of MZO alloys from first principle calculation (Maznichenko *et al*., 2009). They concluded that the phase transition from the wurzite to the rocksalt structure is predicted at the Mg concentration of $x = 0.33$, which is closed to the mixed phased regime observed experimentally.

1.3   Research objectives

a) Explore the possibility of synthesis $Mg_xZn_{1-x}O$ nanocrystals by an oxalate-based coprecipitation method.

b) Study the conditions of structural phase transition from wurtzite structure of ZnO to rocksalt structure of MgO.

c) Study the local structure of $Mg_xZn_{1-x}O$ nanocrystals by x-ray absorption spectroscopy.

d) Study the synthesis $Mg_xZn_{1-x}O$ products by characterization tools available in SUT, Nano-KMITL and SLRI. The characterization techniques used in this study are X-ray diffraction (XRD), Scanning electron microscope (SEM), Transmission electron microscope (TEM), Ultraviolet-visible spectroscopy (UV-VIS), and X-ray absorption spectroscopy (XAS).

1.4   Scope and limitation of the study

This study is a preliminary research aiming to find an economic way to synthesize $Mg_xZn_{1-x}O$ nanocrystals. The synthesized products may not only be $Mg_xZn_{1-x}O$ but at least we will identify the chemical species of the product using the available tools. The local structure of $Mg_xZn_{1-x}O$ nanocrystals will be characterized by XAS. FEFF 8.2 code will be used to simulate the x-ray absorption near edge structure (XANES) of $Mg_xZn_{1-x}O$ nanocrystals to compare with experiment.

CHAPTER II

RESEARCH METHODOLOGY

In this chapter, the research methodology utilized in the thesis work will be reviewed. Firstly, x-ray diffraction (XRD) was used for the structural characterization of $Mg_xZn_{1-x}O$ products. Secondly, by the scanning electron microscope (SEM) equipped with energy dispersive spectroscopy (EDS) was used for alloys composition determination, then transmission electron microscope (TEM) was used for taking the high resolution micrograph of nano-crystals. The ultraviolet-visible spectroscope (UV-VIS) was used to study the optical band edge absorption. Next, the attention was focused to the study of local structure around specific atoms which can be done by using x-ray absorption spectroscopy (XAS) in both extended x-ray absorption fine structure (EXAFS) and x-ray absorption near-edge structure (XANES) regions. We will describe the general concept of those techniques and on how to extract the result from experiments. Finally, the detail of XAS spectrum calculation will be discussed in the last section.

2.1 Oxalate-based co-precipitation method

2.1.1 Preparation of $Mg_xZn_{1-x}O$ alloys

Zinc acetate, Magnesium acetate and Oxalic acid were used as starting materials. Initially, the mixed oxalate precursors $Mg_xZn_{1-x}(C_2O_4)\cdot 2H_2O$ ($x = 0$, 0.01, 0.04, 0.06, 0.10, 0.15, 0.25, 0.30, 0.35, 0.50, 0.70, 0.80, 0.90) were prepared by

adding 0.4 mol solutions of zinc and magnesium acetates with a 0.4 mol solution of oxalic acid. The adding speed of the aqueous solutions of zinc and magnesium acetates was about 15 ml/min. The precipitates were washed with de-ionized water, dried at 60°C for 4 h, and transformed to $Mg_xZn_{1-x}O$ by heating in air at 550°C for 24 h. The procedure is shown in Figure 2.1.
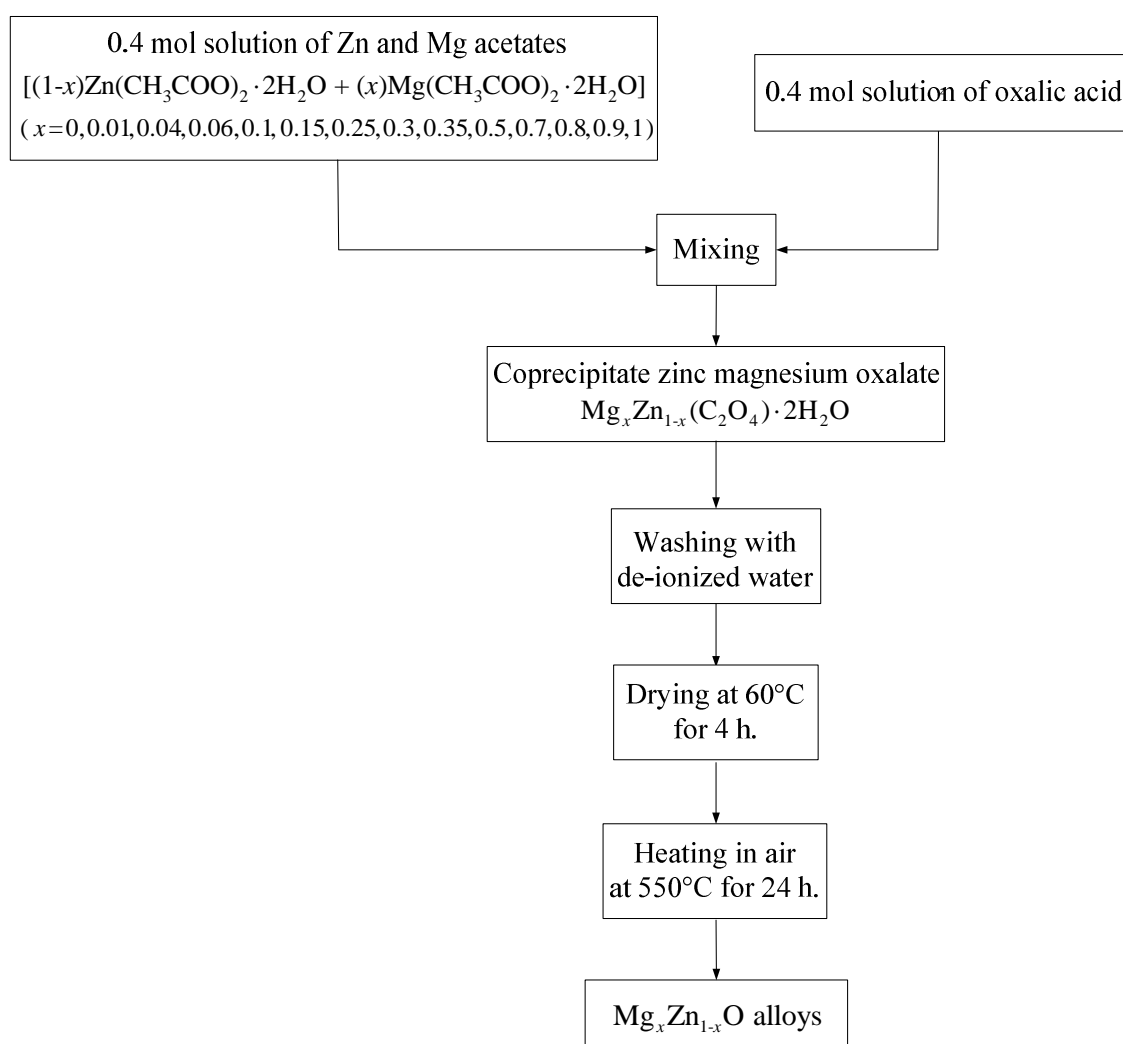
Figure 2.1 Process diagram for the synthesis of $Mg_xZn_{1-x}O$ nanocrystals.

2.2   X-ray powder diffractometry (XRD)

X-ray powder Diffraction is a one of the standard technique that can be used to identify the crystal structure of material. Fundamental treatment of x-ray diffraction by crystals is done by considering the interaction of an x-ray plane wave with the electrons of the crystal materials (Guinier, 1994). The wave nature of the x-rays means that they are reflected by the lattice of the crystal, as shown in Figure 2.2, to give a unique pattern of peaks of "reflections" at differing angles and of different intensity, just as light can be diffracted by a grating of suitably spaced lines. The diffracted beams from atoms in successive planes cancel unless they are in phase, and the condition for this is given by the Bragg relationship;

$$2d \sin \theta \;=\; n\lambda, \tag{2.1}$$

where d is the distance between adjacent planes of atoms, θ is the angle of incidence of the x-ray beam, n is the order of the diffracted beam and λ represents the wavelength of the incident x-ray beam.
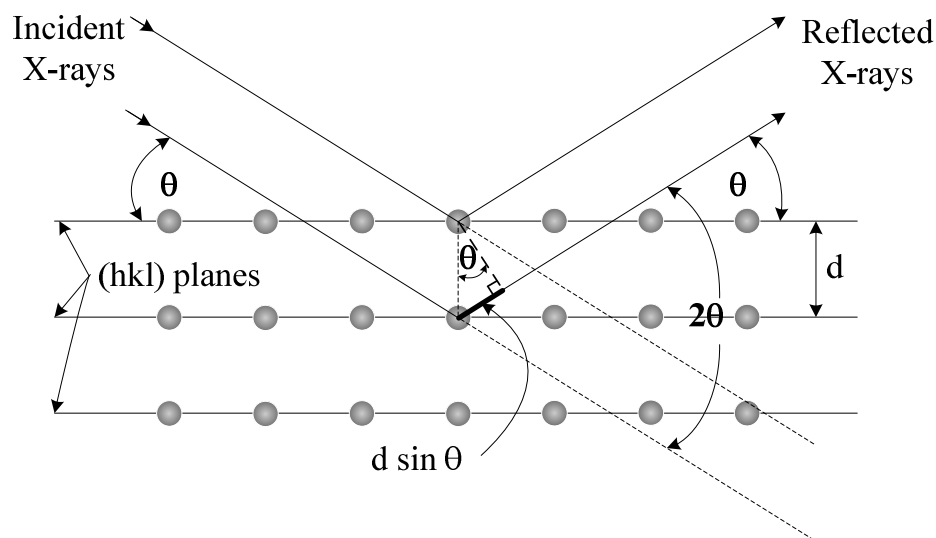
Figure 2.2 The X-ray diffraction beam path.

The Bragg condition can be satisfied for any set of planes whose spacing is greater than half the wavelength of the x-ray used (if d < λ/2, then $\sin\theta > 1$, which is impossible). This condition sets a limit on how many orders of diffracted waves can be obtained from a given crystal using an x-ray beam of a given wavelength. Since the crystal pattern repeats in three dimensions, forming a three-dimensional diffraction grating, three integers, denoted (*h k l*) are required to describe the order of the diffracted waves. These three integers are defined as the Miller indices which used in crystallography, denote the orientation of the reflecting sheets with respect to the unit cell and the path difference in units of wavelength between identical reflecting sheets.

The Miller indices (*h k l*) can be calculated from Bragg's law:

$$2d_{hkl} \sin \theta \ = \ n\lambda . \tag{2.2}$$

In the cubic systems, the plane spacing is related to the lattice parameter and the Miller indices by the following relation:

$$d_{hkl} \ = \ \frac{a}{\sqrt{h^2 + k^2 + l^2}} . \tag{2.3}$$

Combining equation (2.2) and (2.3), we get

$$a_{hkl} \ = \ \frac{n\lambda \sqrt{h^2 + k^2 + l^2}}{2\sin \theta} . \tag{2.4}$$

Considering the non cubic systems such as hexagonal system, the Miller indices can be calculated by using the lattice parameter from Bravais lattice:

$$\frac{1}{d^2} = \frac{4}{3}\left(\frac{h^2 + hk + k^2}{a^2} \right) + \frac{l^2}{c^2} . \tag{2.5}$$

Recall Bragg's law:

$$2d \sin \theta \ = \ \lambda , \tag{2.6}$$

$$4d^2 \sin^2 \theta = \lambda^2 , \tag{2.7}$$

$$\frac{1}{d^2} = \frac{4\sin^2 \theta}{\lambda^2} . \tag{2.8}$$

Combining equation (2.5) and (2.8), we obtain

$$\frac{1}{d^2} = \frac{4}{3}\left(\frac{h^2 + hk + k^2}{a^2}\right) + \frac{l^2}{c^2} = \frac{4\sin^2 \theta}{\lambda^2} . \tag{2.9}$$

We can rearrange equation (2.9) in term of $\sin^2 \theta$ as,

$$\sin^2\theta = \left(\frac{\lambda^2}{4a^2}\right) * \left[\frac{4}{3}(h^2 + hk + k^2) + \frac{l^2}{(c/a)^2}\right], \tag{2.10}$$

where a and c/a are constants for a given diffraction pattern.

The information of an XRD pattern can be used to approximate the crystallite size of particles by using Debye-Scherrer formula (Warren, 1969):

$$D = \frac{K\lambda}{\beta \cos \theta}, \tag{2.11}$$

where D is crystalline size, λ is the wavelength of x-ray radiation (1.5418 Å for Cu K_α), β is the full wide at half maximum height (FWHM), K is the crystallite shape factor (usually taken as 0.89), θ is the diffraction angle.

The x-ray diffraction technique is normally carried out by an x-ray diffractometer. The essential components of x-ray diffractometer (Fultz and Howe, 2008) are:

1) A source of x-ray, usually a sealed x-ray tube

2) A goniometer, which provides precise mechanical motions of the tube, specimen and detector

3) An x-ray detector

4) Electronics for counting detector pulses in synchronization with the positions of the goniometer

There are four practical approaches for observing diffractions and making diffraction measurements: Debye-Scherrer Method, Laue Method, Rotating Crystal Method and θ-2θ diffractometer Method. All are designed to ensure that Bragg's law is satisfied. The schematic diagram of θ-2θ x-ray diffractometer used in this work (BRUKER X-ray diffractometer model D5005 equipped with Cu K_α sealed tube, wave length 1.54 Å) is shown in Figure 2.3 and 2.4. The θ-2θ Diffractometer is used for diffraction measurements of unfixed horizontal sample. For this purpose, sample will be rotated to θ and x-ray detector moved to 2θ. The diffraction angle followed on Bragg's equation (2.1). The one-side weight of the tube stand is compensated by a counter weight. Both tube stand and counter weigh are fixed to the outer ring.
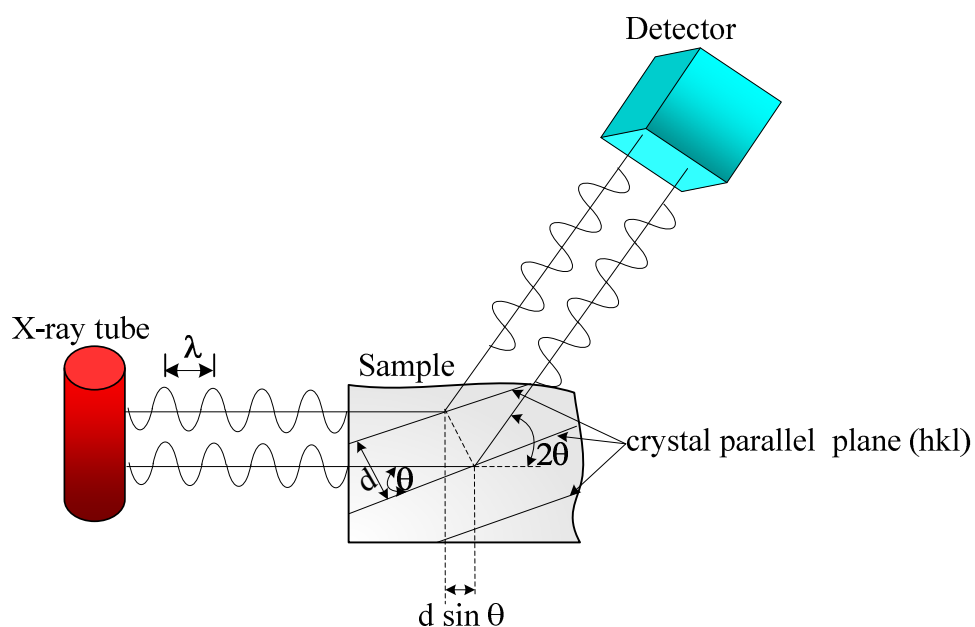
Figure 2.3 Schematic illustration of θ-2θ x-ray diffraction experiment [adapted from (Smith, 1993)].
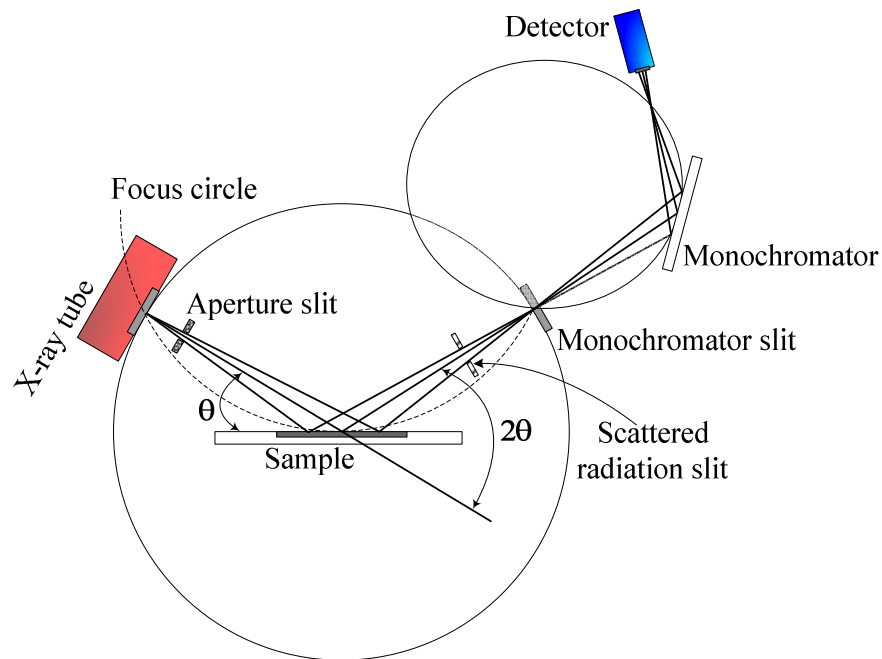
Figure 2.4 Schematic representation of X-ray diffractometer D5005 [adapted from (BRUKER, Analytical X-ray Systems, 1998)].

2.3 Scanning electron microscope (SEM)

The scanning Electron Microscope (SEM) is an importance electron microscope that uses a focused beam of high-energy electrons to generate a variety of signals at the surface of solid specimens. The signals that derive from the interaction of the focused beam of high energy electrons with the atoms of the target sample reveal information about the sample including external morphology (texture), chemical composition, and crystalline structure and orientation of materials making up the sample (Brandon and Kaplan, 1999).

The schematic diagram of scanning electron microscope is shown in Figure 2.5. The SEM generates a beam of incident electrons in an electron column above the sample chamber. The electrons are produced by a thermal emission source, such as a heated tungsten filament, or by a field emission cathode. The energy of the incident

electrons can be as low as 100 eV or as high as 30 keV depending on the evaluation objectives. The electrons are focused into a small beam by a series of electromagnetic lenses in the SEM column. Scanning coils near the end of the column direct and position the focused beam onto the sample surface. The electron beam is scanned in a raster pattern over the surface for imaging. The beam can also be focused at a single point or scanned along a line for x-ray analysis. The beam can be focused to a final probe diameter as small as about 10 Å. when the electron beam strikes a specimen, a large number of signals are generated. Theses signals include secondary electrons, backscattered electrons, characteristic x-ray, cathodoluminescence and transmitted electrons, as shown in Figure 2.6.
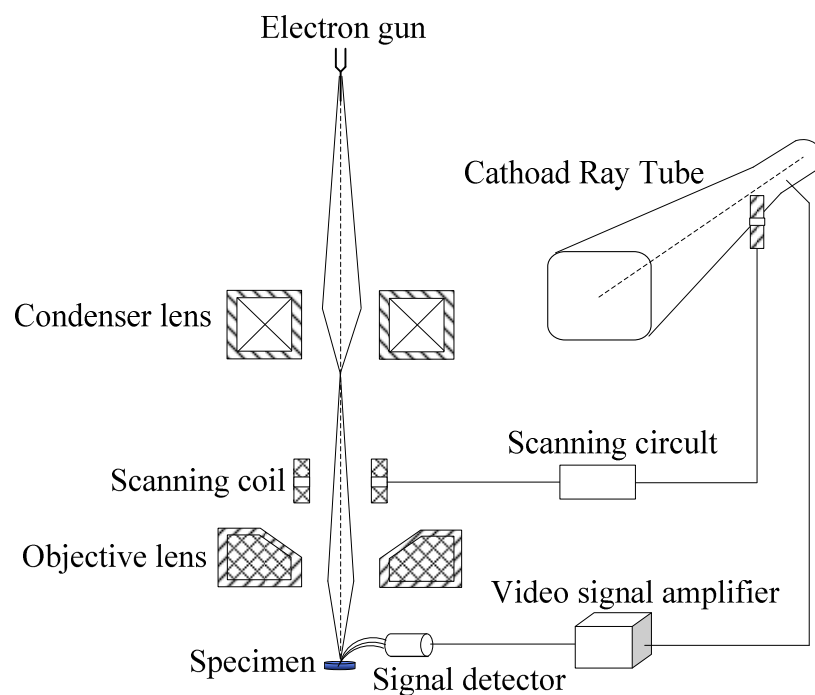
Figure 2.5 Principles schematic illustration of SEM (JEOL, Ltd., 1989).
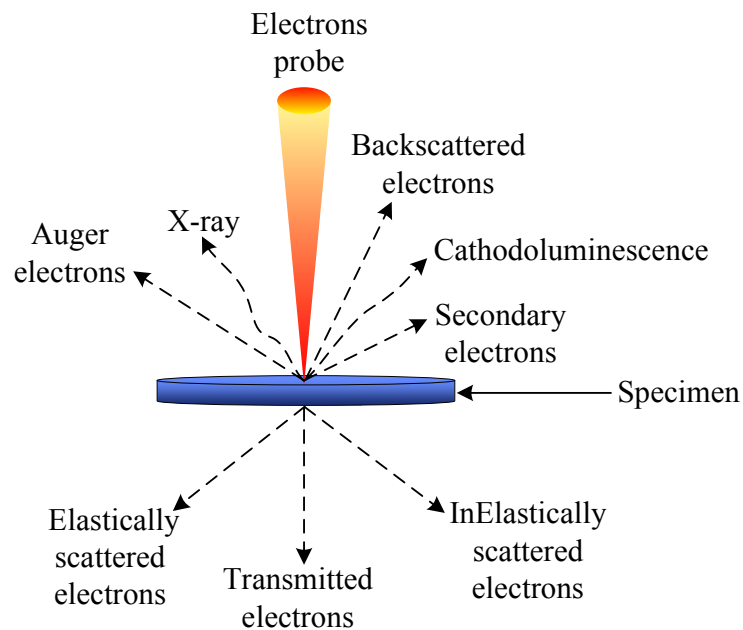
Figure 2.6 Schematic diagram of signals in SEM.

There are four the significant signals which to use in SEM:

1) Secondary Electrons (SE) are emitted lower-energy electrons, which can be formed by inelastic collisions with the nucleus where substantial energy loss occurs or by the ejection of loosely bound electrons from the sample atoms. The energy of secondary electrons is typically 50 eV or less. The topography of surface features influences the number of electrons that reach the secondary electron detector from any point on the scanned surface. This local variation in electron intensity creates the image contrast that reveals the surface morphology. The secondary electron image resolution for an ideal sample is about 3.5 nm for a tungsten-filament electron source SEM or 1.5 nm for field emission SEM.

2) Backscattered electrons are high-energy electrons that are ejected by an elastic collision of an incident electron, typically with a sample atom's nucleus. These high-energy electrons can escape from much deeper than secondary electrons, so surface topography is not as accurately resolved as for secondary electron imaging.

The production efficiency for backscattered electrons is proportional to the sample material's mean atomic number, which results in image contrast as a function of composition, mean that higher atomic number material appears brighter than low atomic number material in a backscattered electron image. The optimum resolution for backscattered electron imaging is about 5.5 nm.

3) Characteristic x-rays are generated when the electron beam interacts with the inner shell electrons of the specimen atoms by inelastic scattering with enough energy to excite inner shell electrons to outer shell orbitals, leaving inner-shell vacancies. As outer-shell electrons fall to the various inner shell orbitals, characteristic amounts of energy are generated that are a function of the target element and the type of orbital decay. These characteristic x-ray are used to identify the component and measure the plenty of elements in the sample.

4) Cathodoluminescence (CL), the emission of light when atoms excited by high-energy electrons come back to their ground state. In the SEM, CL detectors either collect all light emitted by the specimen, or can analyse the wavelengths emitted by the specimen and display an emission spectrum or an image of the distribution of cathodoluminescence emitted by the specimen in real colour.

To create an SEM image, the incident electron beam is scanned in a raster pattern across the sample's surface. The emitted electrons are detected for each position in the scanned area by an electron detector. The intensity of the emitted electron signal is displayed as brightness on a cathode ray tube (CRT). By synchronizing the CRT scan to that of the scan of the incident electron beam, the CRT display represents the morphology of the sample surface area scanned by the beam. Magnification of the CRT image is the ratio of the image display size to the sample area scanned by the electron beam.

Two electron detector types are predominantly used for SEM imaging. Scintillator type detectors (Everhart-Thornley) are used for secondary electron imaging. This detector is charged with a positive voltage to attract electrons to the detector for improved signal to noise ratio. Detectors for backscattered electrons can be scintillator types or a solid-state detector. The SEM column and sample chamber are at a moderate vacuum to allow the electrons to travel freely from the electron beam source to the sample and then to the detectors. High-resolution imaging is done with the chamber at higher vacuum, typically from 10^{-5} to 10^{-7} Torr. Imaging of nonconductive, volatile, and vacuum-sensitive samples can be performed at higher pressures.

Energy dispersive x-ray spectroscopy (EDS) is an analytical technique for identifying and quantifying elemental compositions in a very small sample of material. EDS is an integral part of the scanning electron microscope. When taking an SEM image, the surface under consideration is bombarded with an electron beam. A schematic of EDS system is depicted in Figure 2.7. The bombardment of electrons causes an excitation between the atoms, which results in a release of excess energy in the form of X-ray. When the samples surface is bombarded by the electron beam, some electrons are removed from the atoms on the sample surface. This results in electron vacancies which must be filled with electrons from a higher shell. As a result, an X-ray is emitted to balance the energy difference between the two electrons. The amount of energy released is characteristic of the atoms it excites, forming various peaks in the energy spectrum, according to the composition of the material. The intensities or areas of the various peaks of a specific spectrum are proportional to the concentration of that specific element, making EDS not only a qualitative but also a quantitative composition diagnostics tool.
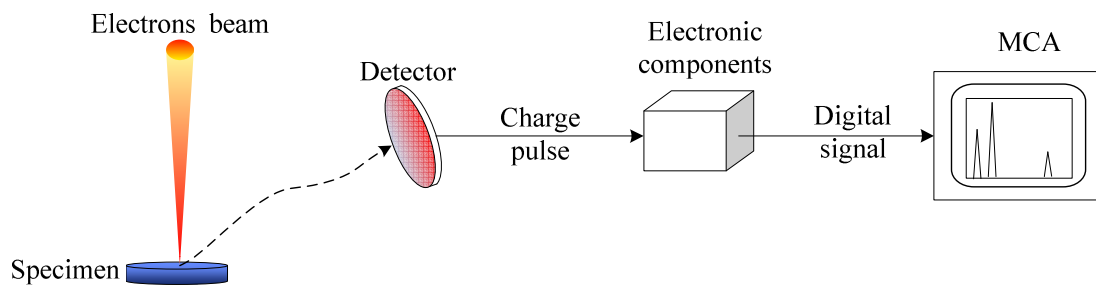
Figure 2.7 Schematic diagram of an EDS.

2.4 Transmission electron microscopy (TEM)

Transmission electron microscopy is a microscopy technique that uses a high energy electron beam transmitted through a very thin specimen and analyzed the microstructure of materials with atomic scale resolution. The high energy electrons from the gun are focused with electromagnetic lenses and the image is formed from the interaction of the electrons transmitted through the specimen and scattered is observed after being magnified by electron lenses. The electron-intensity distribution behind the specimen is imaged with a three or four-stage lens system, onto a fluorescent screen that converts the high energy electron image into an image that is visible to the eye. The image can be recorded by direct exposure of a photographic emulsion inside the vacuum or digitally by CCD or TV cameras. TEM has a greater resolving power than a light-power optical microscope, because it uses electrons that have wavelength about 100,000 times shorter than visible light (photons), and can achieve magnifications of up to 20,000x, whereas light microscopes are limited to 2,000x magnification.

For optical microscope, the resolution (d) has been limited by the wavelength of the photons that are being used to probe the sample (λ) with the relationship (Brandon and Kaplan, 1999);

$$d = \frac{0.61\lambda}{\mu \sin \alpha},$$ (2.12)

where μ is the refractive index of the medium between the sample and the objective lens. The product, $\mu \sin \alpha$ is usually called the numerical aperture (NA).

Electrons have both wave and particle properties and their wave-like properties thus wavelength, λ, and momentum, p, are related by the de Broglie relationship;

$$\lambda = \frac{h}{p},$$ (2.13)

where h is the Planck constant. In the TEM, the de Broglie relationship is not sufficient to define the wavelength of an electron at high energies because relativistic effects become important at these energies. If the rest mass of electron is m_0 and assuming that the accelerating voltage in the electron gun is V. Hence, the relativistic equation for the wavelength of the electron λ_e in term of the accelerating voltage as

$$\lambda_e = \frac{h}{\sqrt{2m_0 eV(1 + eV/2m_0 c^2)}}.$$ (2.14)

TEM is comprised of the several components, which include a vacuum system in which the electrons travels. Schematic representation of TEM was shown in Figure 2.8. At the top of the instrument is the electron gun, which is the source of electrons. The electrons are emitted in the electron gun by thermionic emission from tungsten hairpin cathodes or lanthanum hexaboride (LaB_6) rods or by field emission from pointed tungsten filament. Then, the electrons are accelerated to high energies (typically 100-400 keV) and focused towards the specimen by a two-stage condenser-

lens system. The condenser aperture used to control the convergence angle of the beam. The objective lenses focus the beam down to the sample, while the projector lenses are used to expand the beam onto the fluorescent screen or other imaging device. The magnification of the TEM is due to the ratio of the distance between the specimen and the objective lenses image plane. An image is formed from the transmitted beam, which contains information about electron density, phase and periodicity.
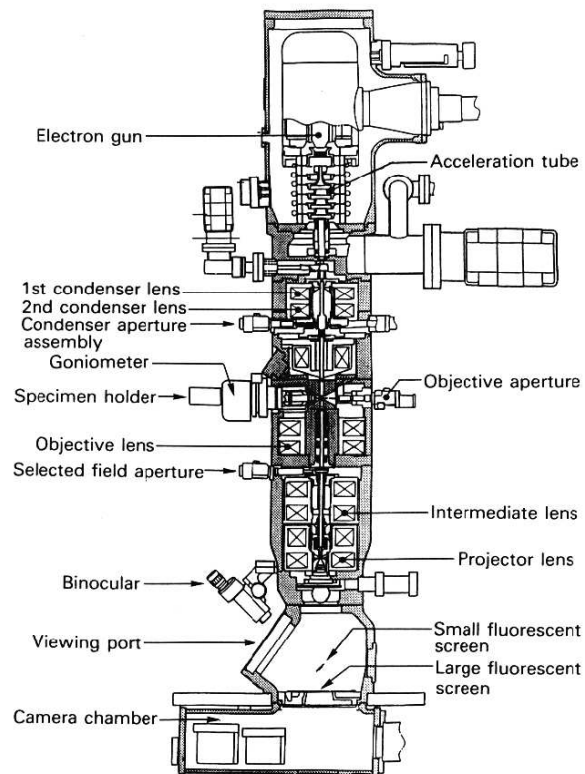
Figure 2.8 Cross section of column in Transmission electron microscope (Fultz and Howe, 2008).

Phase-contrast imaging is the highest resolution imaging technique in TEM, which can be used to investigate the crystal structure of materials. This technique arises from the fact that the atoms in a material diffract electrons as the electrons pass

through them, causing diffraction contrast in addition to the already present contrast in the transmitted beam. In the central section of TEM the electron beam interacts strongly with specimen by elastic and inelastic scattering. The specimen must therefore be very thin, typically of the order of 5 nm-0.5 μm for 100 keV, depending on the density and elemental composition of the object and the resolution desired.

Electron diffraction (ED) is the one of significant diffraction techniques of three groups, X-ray diffraction, Neutron diffraction, and electron diffraction. Diffraction in transmission electron microscopy used technique known as "Selected Area Electron Diffraction, SEAD". This technique can easily choose from which part of the specimen to obtain the diffraction pattern. In TEM, the interactions of the electron beam with planes of specimen and produced small angles lead to electron diffraction. An electron of diffraction from planes of atom in specimen will be focused by objective lens at diffraction points.

TEM can provide two separate kinds of information about a specimen, a magnified image and a diffraction pattern. The objective lens forms a diffraction pattern in the back focal plane with electrons scattered by the specimen and combines them to generate an image in the image plane. Thus, diffraction pattern and image are simultaneously present in TEM. It depends on the intermediate lens which of them appears in the plane of the second intermediate image and magnified by the projective lens on the viewing screen. Switching from real space (image) to reciprocal space (diffraction pattern) is easily by achieved by changing the strength of the intermediate lens. Ray diagrams of image and diffraction pattern as presented in Figure 2.9.
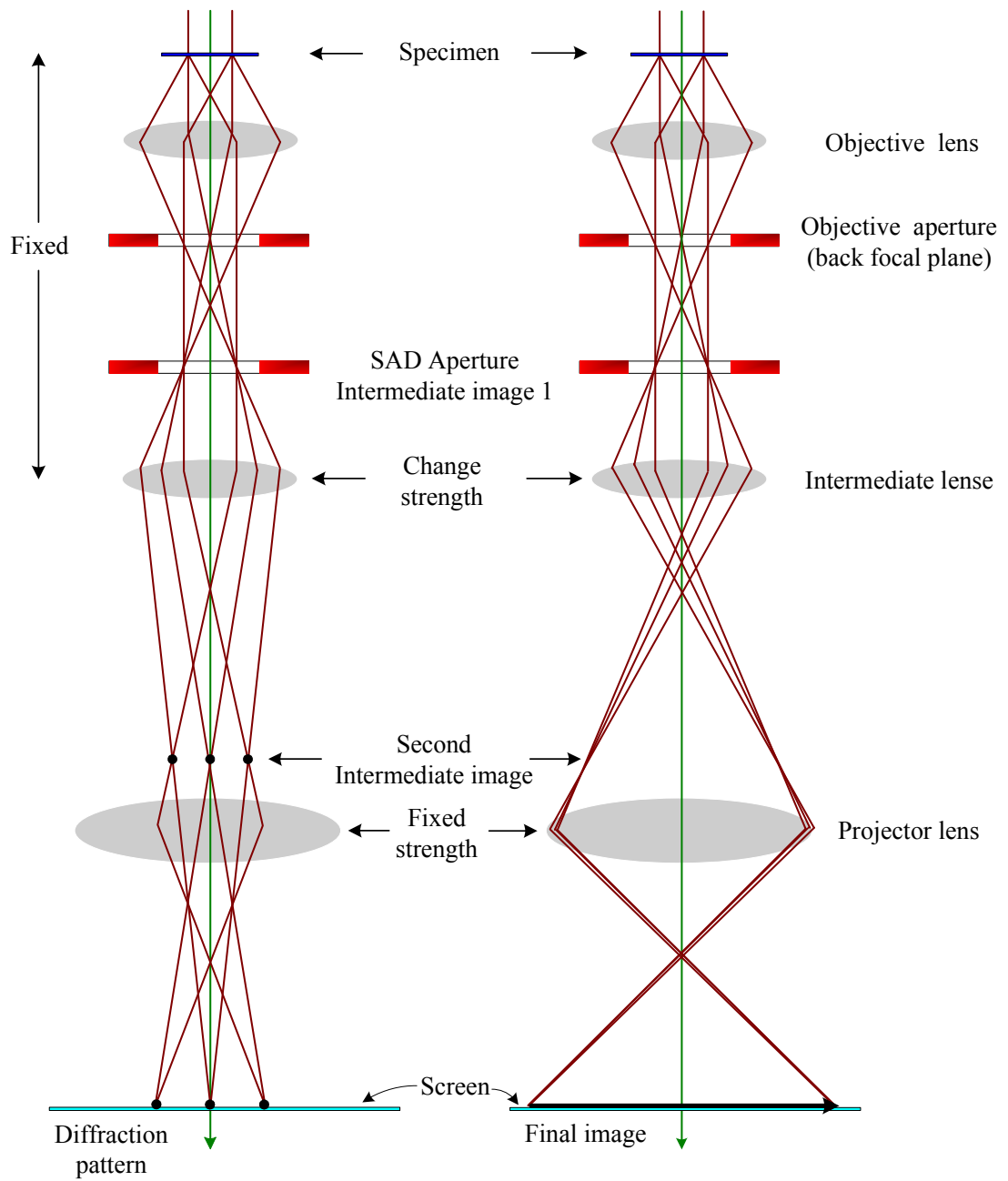
Figure 2.9 Ray diagrams of (a) diffraction pattern and (b) image [adapted from (Williams and Carter, 1996)].

(a)

(b)

(c)
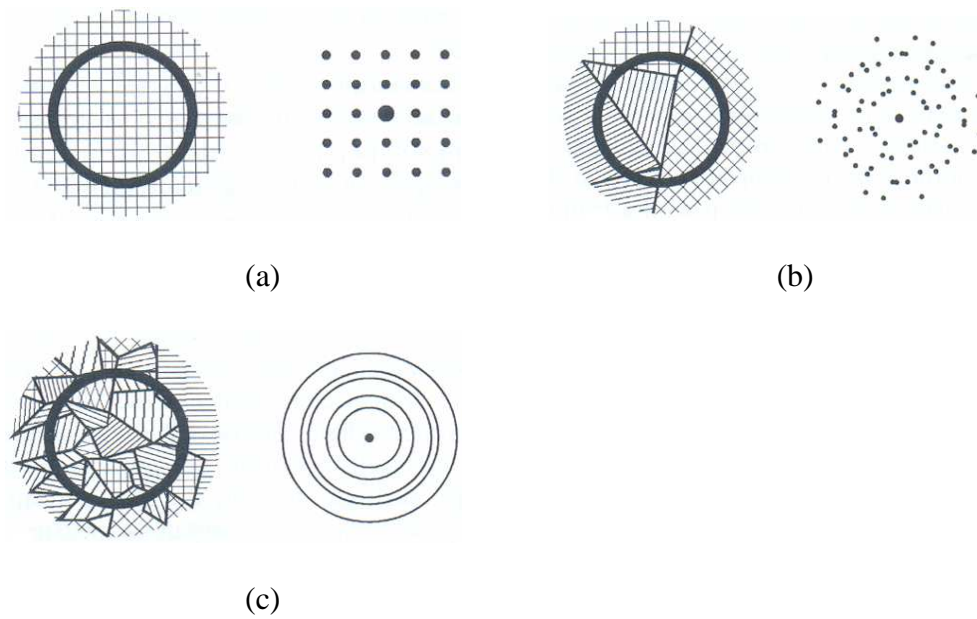
Figure 2.10 Type of diffraction pattern which arise from difference specimen microstructure (a) A single perfect crystal (b) A small number of grains (c) A large number of randomly oriented.
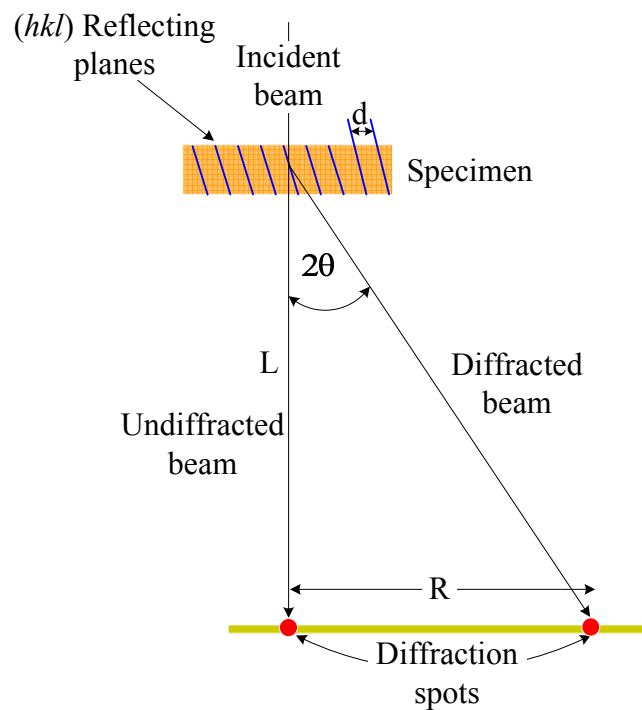
Figure 2.11 Schematic diagram showing the geometry of diffraction pattern formation.

In imaging mode, an objective aperture can be inserted in the back focal plane to select one or more beams that contribute to the final image. For selected area electron diffraction, an aperture in the plane of the first intermediate image defines the region of which the diffraction is obtained.

A single crystal specimen oriented such that several sets of planes are parallel to the beam will give rise to a diffraction pattern consisting of a regular array spots, as shown in Figure 2.10(a). This pattern provides the investigator with information about the space group symmetries in the crystal and the crystal's orientation to the beam path. If the specimen contains several crystals of different orientations, as shown in Figure 2.10(b), then the diffraction pattern is the sum of the individual, and is more complicated. Figure 2.10(c) shows the case for a specimen containing very many crystals of random orientation. In this situation, the spots on the ring are so close together that the rings appear continuous.

In order to understand the geometry of electron diffraction, we can ignore the lens system, which merely magnifies the diffraction pattern, and consider the much simpler ray diagram of Figure 2.11. A beam of electrons impinges on a crystalline specimen. Some of the electrons pass through the specimen without interaction, and hits the screen which is at a distance L from the specimen, at O. Other electrons are diffracted through an angle 2θ by the crystal planes of spacing d, and these electrons hit the film at A, which is a distances r from O. For the first diffraction spot and θ is small, we get:

$$\sin\theta \approx \tan\theta \approx \frac{1}{2}\tan(2\theta). \tag{2.15}$$

Thus, Bragg's equation (2.1) becomes

$$2d\left(\frac{1}{2}\tan 2\theta\right) = \lambda. \tag{2.16}$$

By the simple geometry used in Figure 2.11:

$$\tan 2\theta = \frac{r}{L}, \tag{2.17}$$

combining equation (2.16) and (2.17), we obtain

$$2d\left(\frac{r}{2L}\right) = \lambda, \tag{2.18}$$

$$rd = \lambda L. \tag{2.19}$$

As the camera length, L, and the wavelength of the TEM accelerating voltage, λ, are dependent of the specimen, and are a constant for the instrument. The product λL is called the Camera Constant. It can be seen that the distance of a diffraction spot from the undiffracted spot, R, is therefore inversely proportional to the lattice spacing, d, of the reflecting planes. If we know the camera constant for instrument, then we can determine the crystal lattice spacing simply by measuring the distances between spots on a single crystal diffraction pattern, or ring diameters on polycrystalline diffraction pattern.

2.5 Ultraviolet-visible (UV-VIS) spectroscopy

The ultraviolet-visible (UV-VIS) spectroscopy refers to absorption spectroscopy, which is an instrument commonly used in the laboratory that analyzes compounds in the ultraviolet (UV) and visible (Vis) regions of the electromagnetic spectrum (Rouessac, 2004). The absorption in the visible region directly affects the perceived color of the chemical involved. In this region, molecules undergo electronic transitions. This technique measures transitions from the ground state to the excited state and determine the wavelength and maximum absorbance of the compounds. The wavelength and amount of light that a compound absorbs depends on its molecular structure and the concentration of the compound used. A diagram of the components of typical spectrometer is shown in Figure 2.12.
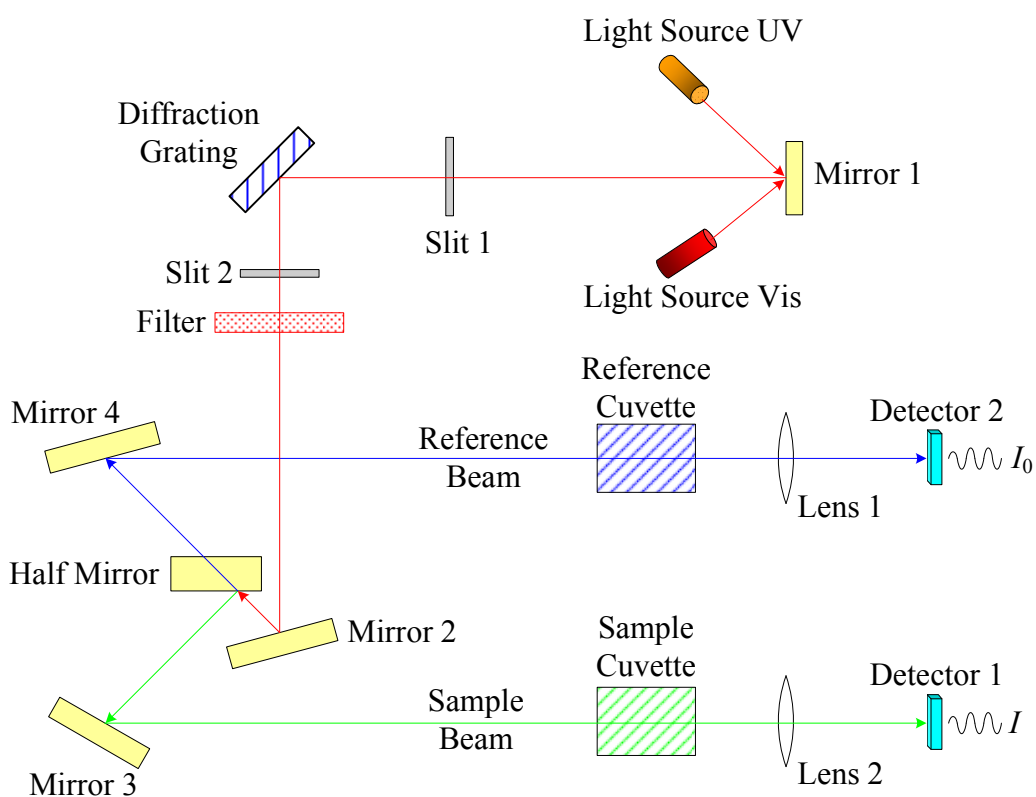
Figure 2.12 A diagram of the components of typical UV-Vis spectrometer.

The functioning of this instrument is relatively straightforward. A beam of light from a visible and UV light source is separated into its component wavelength by a prism or diffraction grating. Each monochromatic beam in turn is split into two equal intensity beams by a half-mirrored device. One beam passes through a small transparent container (cuvette) containing a solution of the compound. The other beam is the reference, which passes through an identical cuvette containing only the solvent. The detector measures the intensity of the reference beam (I_0) and compares it to the intensity of the sample beam (I). Over a short period of time, the spectrometer automatically scans all the component wavelengths in the manner described. The ultraviolet region scanned is normally from 200 to 400 nm, and the visible portion is from 400 to 800 nm. If the sample compound absorbs light then I is less than I_0, and this difference may be plotted on a graph versus wavelength, as shown in Figure 2.13. Absorption may be presented as transmittance (T):

$$T = \frac{I}{I_0}.$$

(2.20)

On the other hand, the absorbance, A, can be calculated from the Beer-Lambert law:

$$A = \log\frac{I_0}{I} = \varepsilon c l,$$

(2.21)

where ε is molar extinction coefficient, c is the concentration of the compound in solution and l is the path length of the sample.

Molar extinction coefficients are specific to particular compounds, therefore UV-Vis spectroscopy can aid one in determining an unknown compounds's identity. Furthermore, absorption of UV or visible light leads to promotion of an electron from ground state to the excited state. The energy of the absorbed photon must be equal to the difference in energy between the ground state and the excited state, which only

photons of a particular frequency (or wavelength) will be absorbed. This energy can be calculated by using the equation:

$$E = \frac{hc}{\lambda},$$
(2.22)

where h is the Planck's constant, c is the speed of light and λ is the wavelength (at the absorption edge). An UV-visible absorption spectrum is shown in figure 2.13.
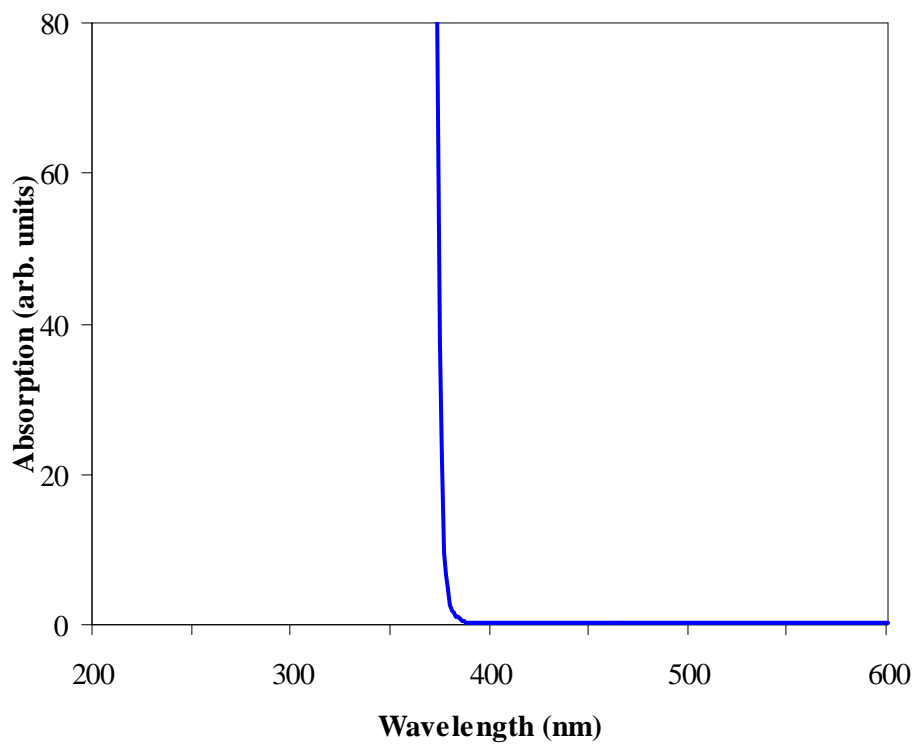
Figure 2.13 UV-visible absorption spectrum of ZnO nanocrystals.

2.6   X-ray absorption spectroscope (XAS)

X-ray absorption Spectroscopy (XAS) is one of the powerful techniques to examine the electronic structure of materials, formal oxidation state, coordination number and used to probe local structure. The XAS experiment is normally carried out at the synchrotron radiation facility, which can be modified and selected the energy of x-ray photon (Koningsberger and Prins, 1988).

X-ray absorption spectroscope measures the x-ray absorption $\mu(E)$ as a function of x-ray energy

$$E = \hbar\omega .\tag{2.23}$$

The x-ray absorption coefficient is determined from the decay in the x-ray intensity I with the length of a sample x by the relationship,

$$I = I_0 e^{-\mu x},\tag{2.24}$$

where I_0 is the intensity of the incoming x-ray beam, I is the intensity of the beam after pass though the sample, and x is the thickness of the sample, μ is the definition of absorption coefficient, as shown in Figure 2.14.
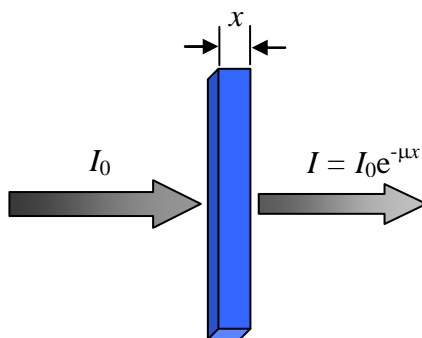
Figure 2.14 Schematic view of x-ray absorption measurement in transmission mode.

In the x-ray absorption process, a photon is absorbed by the atom, giving rise to the transition of the electrons from the inner shells: K, L or M shell to empty state above the Fermi level. The core hole, empty state, will be created in the inner shell, and the energy level of the shell is used to identify the type of absorption edge as shown in Figure 2.15. For example, K-edge refers to transition that excited electron from 1s shell to unoccupied states. The x-ray photon energy has to greater than the difference of energy between unoccupied states and K shell state. The energy of the absorption edges are specific characteristic to elements, making x-ray absorption an element-selective technique.
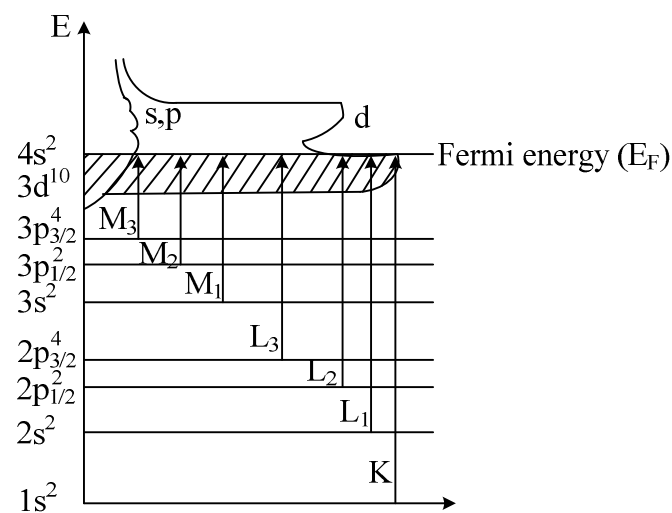
Figure 2.15 The relationship between the energy transitions and absorption edges [adapted from (Rehr and Albers, 2000)].
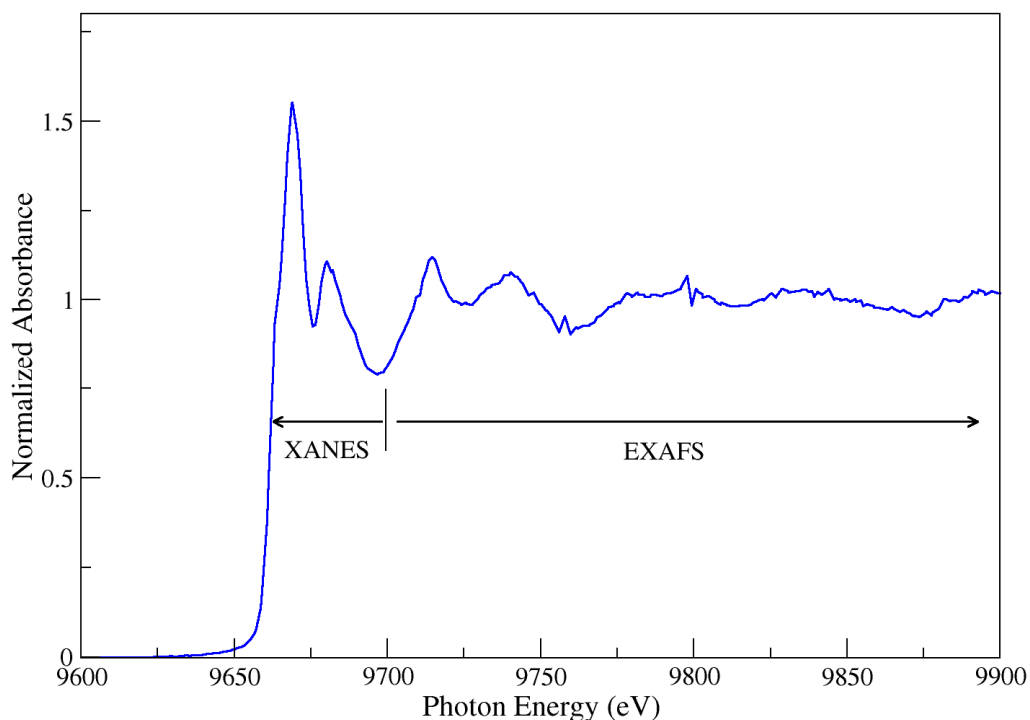
Figure 2.16 Normalize Zn *K*-edge absorption spectra classified into two regions; XANES and EXAFS.

The x-ray absorption spectrum is typically separated into two regions (1) the x-ray absorption near edge structure (XANES) which includes features approximately 50 eV above the absorption edge and (2) the extended x-ray absorption fine structure (EXAFS) typically extending to 1,000 eV above the absorption edge as shown in Figure 2.16.

2.6.1 X-ray absorption near edge structure (XANES)

X-ray absorption near edge structure, or XANES contains the information about the chemical state of the element, including the oxidation state, and the local geometry of the absorbing atom. XANES structure in an absorption spectrum cover the range between the threshold and the point at which the extended x-ray absorption

fine structure (EXAFS) being. XANES comprises that part of the spectrum within about 40-50 eV of the edge.

In this region of the absorption spectrum is dominated by multiple scattering of low energy of photoelectron. In addition there are normally strong features due to transitions to empty bonding and anti-bonding orbitals in molecular systems, or to atomic-like or unoccupied density of state in solid state systems. The combination of these influence mean that XANES is sensitive to the local electronic structure of the absorbing species and the coordination geometry. XANES has most often been used in a fingerprint fashion, with spectra compared to standards to determine the quantity of interest such as the oxidation state of the absorbing element.

The absorption coefficient in equation (2.24) is proportional to the transition rate as given by Fermi's Golden Rule; described by

$$\tilde{\mu}(E) \propto \sum_f \left| \left\langle f \left| \hat{\varepsilon} \cdot \vec{r} \right| i \right\rangle \right|^2 \delta\left(E_i - E_f + \hbar\omega\right), \qquad (2.25)$$

where $|i\rangle$ is the initial core *ket* state vector, $\langle f|$ is the final *bra* state vector of the excited electron, E is the energy of absorbed x-ray photon, E_i is the energy of initial state, E_f is the energy of final state, $\hbar\omega$ is the energy of x-ray photon energy, $\hat{\varepsilon}$ is the x-ray polarization vector and $\tilde{\mu}(E)$ is absorption coefficient with ignoring of core hole life time and experimental resolution (Ankudinov *et al.*, 1998). By considering Eq. further with the additional effects of core-hole life time and experimental resolution, the XANES spectra can be calculated as described later in section 2.7.

2.6.2 Extended x-ray absorption fine structure (EXAFS)

The extended x-ray absorption fine structure is the oscillating part of the x-ray absorption spectrum that extends to about 1,000 eV above the absorption edge. Analyses of the <u>EXAFS spectrum provide information about the number, species and inter-atomic distances of the neighbors from the absorption atom</u>. EXAFS is a result of the adjustment of the photoelectron final state due to scattering by the surrounding atoms. The final state photoelectron is changed to first order by a single scattering from each surrounding atom. According to quantum theory this photoelectron can be visualized as a wave emitted form the absorber with wavelength λ is given by the de Broglie relation in equation (2.13). In EXAFS region, the momentum of the photoelectron p can be defined by the free electron relation

$$\frac{p^2}{2m} = h\nu - E_0 , \tag{2.26}$$

where $h\nu$ is the energy of frequency ν photon, E_0 is the bonding energy of the photoelectron and m is mass of the excited electron.

For a solitary atom the photoelectron can be revealed as an outgoing wave as shown in Figure 2.17 by the solid line of Mg atom. The outing wave is scattered by neighbor that surround the absorbing atom and generate scattered wave, which display by the dashed lines of O atoms. The final state is the superposition of the outgoing and scattered waves. Interference occurs between the outgoing and the backscattered waves and then creates the total amplitude. The total amplitude of the electron wave function would be raised or diminished, respectively, thus altering the possibility of absorption of the x-ray correspondingly. The phase change with the wavelength of the photoelectron depends on the distance between the center atom and backscattering atom. The variation of the backscattering strength as a function of energy of the

photoelectron depends on the type of atom doing the backscattering. Thus EXAFS contains information on the atomic surroundings of the center atom.
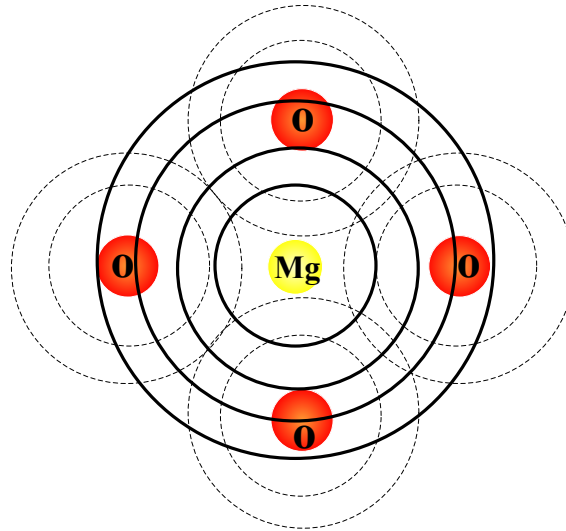
Figure 2.17 Schematic of the radial portion of the photoelectron wave.

The oscillatory part of the x-ray absorption above a given absorption edge, EXAFS function can be defined by

$$\chi(E) = \frac{\left[\mu(E) - \mu_{\circ}(E)\right]}{\Delta\mu_{\circ}}, \tag{2.27}$$

where $\mu(E)$ is the x-ray absorption coefficient, $\mu_0(E)$ is smooth atomic background absorption coefficient.

Furthermore, in the EXAFS analysis $\chi(E)$ could be transformed from E space to k space by the relations $k = \sqrt{2m(E - E_0)/\hbar^2}$. Then the function can be converted from $\chi(E)$ to $\chi(k)$ for general purpose. In theoretical procedure, the $\chi(k)$ can be described by (Wilson *et al.*, 2000)

$$\chi(k) = \sum_j \frac{S_\circ^2 N_j}{k R_j^2} \left| f_j(k,\pi) \right| \sin\left[2kR_j + \varphi_j(k) \right] e^{-2\sigma_j^2 k^2} e^{-2R_j/\lambda(k)} , \qquad (2.28)$$

where N_j is the number of neighbor in j^{th} shell of surrounding atoms, k is photoelectron wave vector, f_j is the scattering amplitude, $S_\circ^2(k)$ is the amplitude reduction term due to many-body effect, R_j is radial distance from absorbing atom to j shell, $\lambda(k)$ is electron mean free path, σ_j is the Debye-Waller factor and $\varphi(k)$ accounts for the total phase shift of the curve wave scattering amplitude along the scattering trajectory.

The distance between core atom and backscattering atoms or the path-length change the phase contrasting with the wavelength of photoelectron. Furthermore, different types of surrounding atoms vary the backscattering intensity as a function of photoelectron energy. It is accepted that, by the careful analysis of the EXAFS structure, one can receive significance structural parameters surrounding the center atom.

2.6.3   X-ray absorption Spectroscopy experimental set up

The x-ray absorption spectroscopy experiment is commonly accomplish at a synchrotron radiation source, due to high intensity and energy alterable competency of generated x-ray photon, and the competency to obtain the continuous absorption spectrum over extensive energy range. In general, there are three types of x-ray absorption measurements: transmission-mode XAS, fluorescence-mode XAS and electron-yield XAS as schematic illustration shown in Figure 2.18.

sample

Incident x-ray
photon beam $\quad I_0 \quad \longrightarrow \quad$ sample $\quad I \quad \longrightarrow \quad$ transmitted x-ray
photon beam

(a)

Incident x-ray
photon beam $\quad I_0 \quad \longrightarrow$

Fluorescence x-ray

X-ray detector

(b)

e^-

Incident x-ray
photon beam $\quad I_0 \quad \longrightarrow$

A

(c)
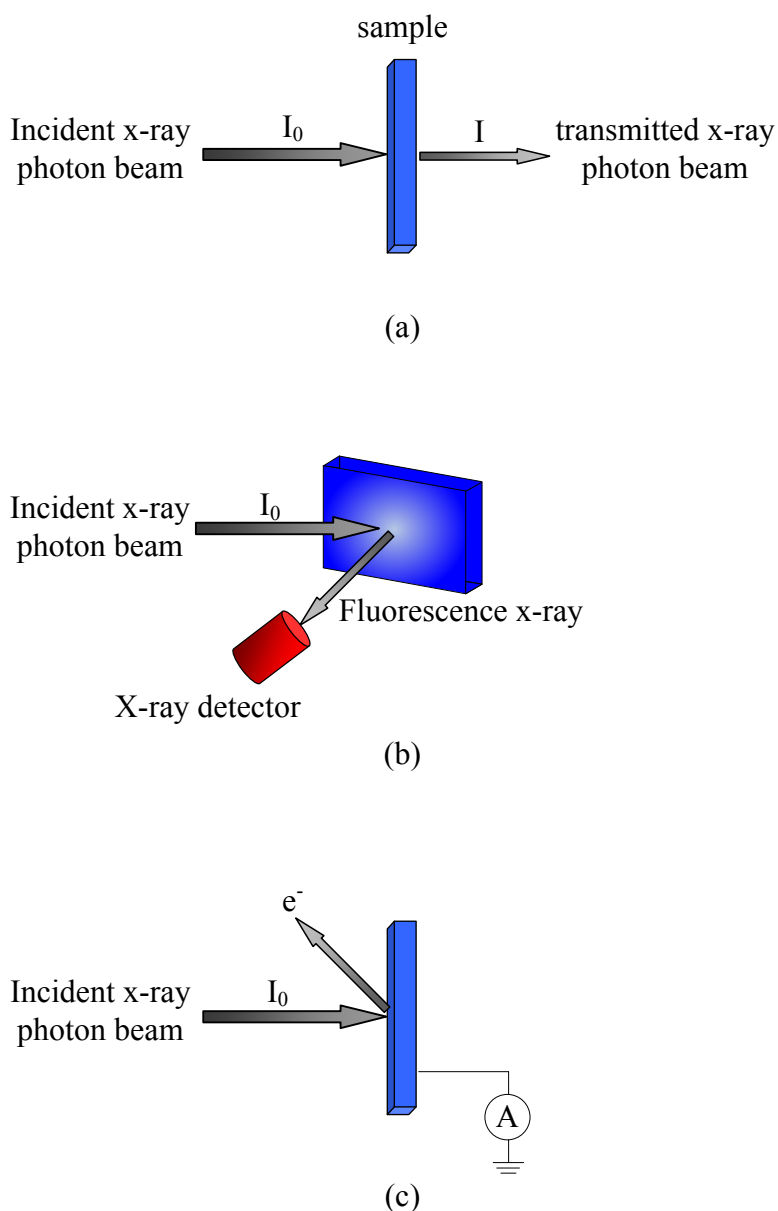
Figure 2.18 The three modes of XAS measurement (a) transmission mode, (b) fluorescence mode and (c) electron yield [adapted from (Kawai, 2000)].

In transmission mode XAS, after the energy of x-ray photons being changed by x-ray double crystals monochromator, the intensities of incident x-ray photon beam (I_0) and the transmitted x-ray photon beam (I) are measured by ionization chambers as shown in Figure 2.19. In this mode, we make sure the x-ray photon beam is well-

aligned on the sample. The x-ray absorption can be extracted based on equation (2.24). The experimental set up of XAS experimental station at XAS beam line, Siam Photon Laboratory, SLRI is shown in Figure 2.20.
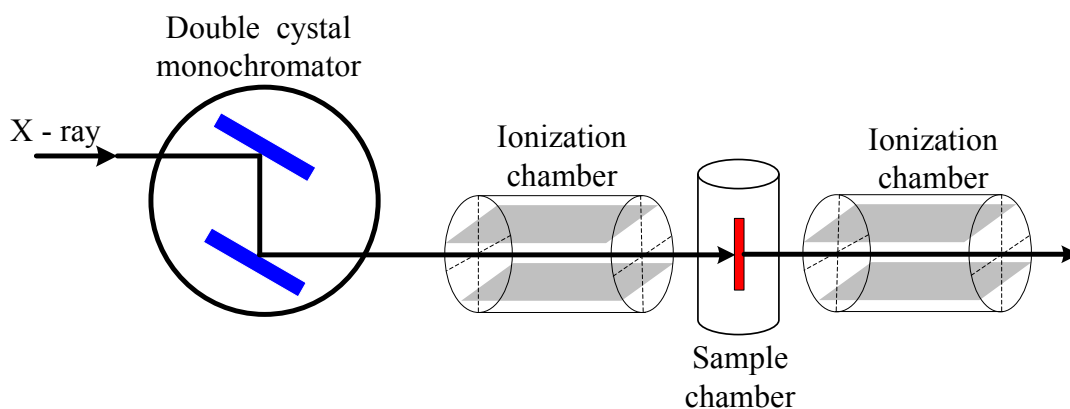
Figure 2.19 Schematic illustration of the experimental setup of transmission-mode X-ray absorption spectroscopy.
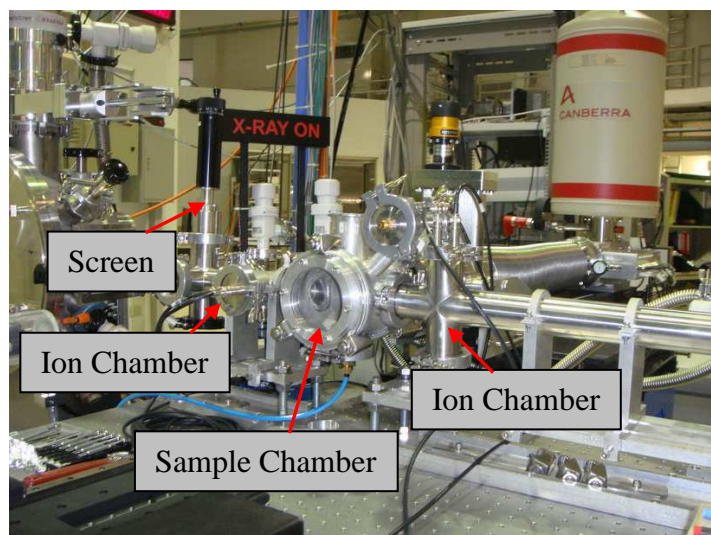
Figure 2.20 XAS experimental set up at the Siam Photon Laboratory, Synchrotron Light Research Institute.

Other than the transmission mode, the fluorescence mode and the electron yield are also competent for the measurement of the absorption coefficient. In the x-ray absorption phenomena, where x-ray photon knock out an electron from the inner shell an electron from higher energy level will cascade down to fill in the hole and discharging radiation of energy, the discharged energy x-ray photon will be released as demonstrated in Figure 2.21(a) and the fluorescence x-ray can be detected. In addition, de-excitation can cause the Auger effect, where the electron reduce to lower energy state, a second electron can be excited to the continuum state and perhaps go out from the sample as shown in Figure 2.21(b), and then we can be detected it by using the electron-yield XAS detectors.

For fluorescence mode, we measure the intensities of incident x-ray photon beam and the fluorescence x-ray that are emitted following the x-ray absorption. Usually the fluorescence detector is placed at 90° to the incident x-ray photon beam in the horizontal plane, with the sample at an angle (usually 45°) with respect to the beam. Fluctuations in the number of elastically scattered x-ray are a significant source of noise in fluorescence XAS, so the position of the detector is selected to minimize the elastically scattered radiation by exploiting the polarization of the x-ray beam. In case of electron yield, we measure the electrons that are emitted from the surface of the sample. The relative short path length (≈ 1000 Å) makes the technique surface-sensitive, which can be beneficial if one is interested in near-surface phenomena. It also can be beneficial for avoiding "self absorption" effect that occurs in fluorescence mode. However, both modes are instantly equivalent to the absorption ability of the sample. Hence, the three techniques are alterable for the study of the structure of material using the absorption ability of the sample.

(a)

(b)
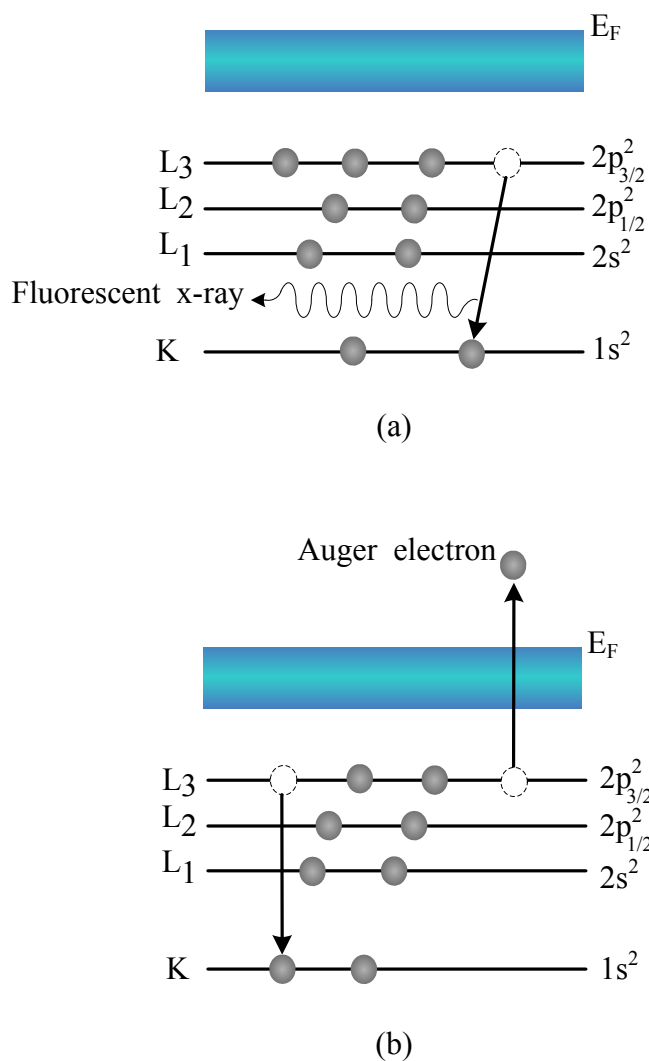
Figure 2.21 The excited state (a) x-ray fluorescence and (b) the Auger effect [adapted from (Koningsberger and Prins, 1988)].

2.7 X-ray absorption spectrum calculation

2.7.1 FEFF code overview

In thesis, the principle theoretical calculations are performed based on FEFF 8.2 code. This code is developed to primarily calculate x-ray absorption for the FEFF (f_{eff}) project developed by the Department of Physics, University of Washington, Seattle. USA. Apart from XAS spectra calculation, FEFF code can also calculate x-

ray natural circular dichroism (XNCD), spin-dependent calculations of x-ray magnetic dichroism (XMCD), nonresonent x-ray emission (XES) and electronic structure including local densities of states (LDOS). FEFF code is written in ANSI FORTRAN 77 with principle investigator John J. Rehr and co-principle investigator Alexei L. Ankudinov.

FEFF is ab intio self-consistent real space multiple-scattering (RSMS) code for simultaneous calculations of x-ray absorption spectra and electronic structure. The input file "feff.inp" can be created directly form ATOMS code via "atoms.inp" as shown in Figure 2.22.


```
title MgO, sodium chloride structure
space  F M 3 M
a=4.213
rmax=10.0
core=Mg
atom
!at.type   x         y         z
   Mg     0.000     0.000     0.000
   O      0.500     0.500     0.500
```
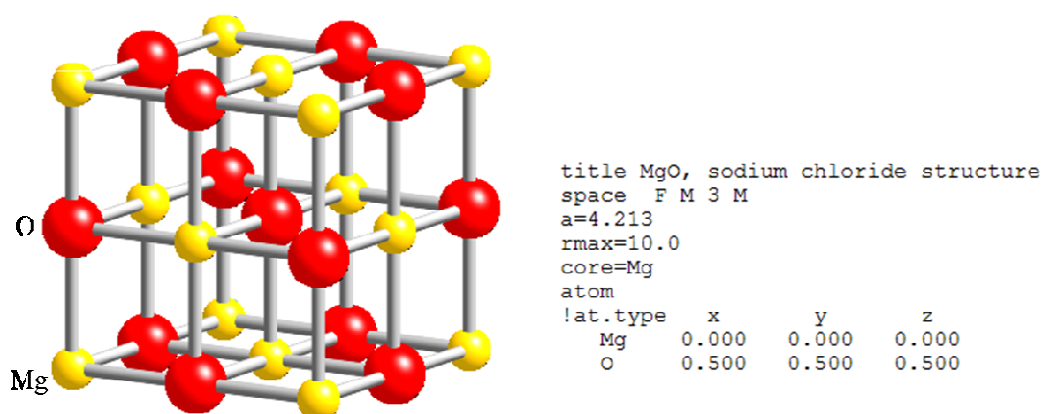
Figure 2.22 Detail of an atoms.inp input file to generate "feff.inp" for FEFF calculation.

```
* This feff.inp file generated by ATOMS, version 2.50
* ATOMS written by and copyright (c) Bruce Ravel, 1992-1999

* -- * -- * -- * -- * -- * -- * -- * -- * -- * -- * -- * -- * -- * -- * -- *
*       total mu =    13646.9 cm^-1, delta mu =      9582.1 cm^-1
*       specific gravity = 3.581, cluster contains  461 atoms.
* -- * -- * -- * -- * -- * -- * -- * -- * -- * -- * -- * -- * -- * -- * -- *
*       mcmaster corrections:  0.00296 ang^2 and  0.210E-04 ang^4
* -- * -- * -- * -- * -- * -- * -- * -- * -- * -- * -- * -- * -- * -- * -- *

TITLE   MgO, sodium chloride structure

EDGE      K
SO2       1.0


*         pot    xsph   fms    paths genfmt ff2chi
CONTROL   1      1      1      1     1      1
PRINT     1      0      0      0     0      0


*         r_scf  [ l_scf  n_scf  ca ]
SCF       4.5       0      15     0.1


*         ixc [ Vr  Vi ]
EXCHANGE  0       0   0

*EXAFS
*RPATH     9.26860


*         kmax  [ delta_k  delta_e ]
XANES     4.0     0.07      0.5
*         r_fms      [ l_fms ]
FMS       8.0          0
*
RPATH     0.10000
*         emin  emax  resolution
*LDOS      -20    20    0.1
POTENTIALS
*   ipot   z [ label   l_scmt  l_fms  stoichiometry ]
      0    12    Mg      -1      -1        0
      1     8    O       -1      -1        1
      2    12    Mg      -1      -1        1

ATOMS
   0.00000      0.00000      0.00000    0  Mg        0.00000
  -2.10650      0.00000      0.00000    1  O         2.10650
   2.10650      0.00000      0.00000    1  O         2.10650
   0.00000      0.00000      2.10650    1  O         2.10650
   0.00000      2.10650      0.00000    1  O         2.10650
   0.00000      0.00000     -2.10650    1  O         2.10650
   0.00000     -2.10650      0.00000    1  O         2.10650
   0.00000      2.10650     -2.10650    2  Mg        2.97904
   0.00000      2.10650      2.10650    2  Mg        2.97904
  -2.10650      2.10650      0.00000    2  Mg        2.97904
                       :
  -6.31950      6.31950      4.21300    2  Mg        9.88036
  -6.31950     -6.31950     -4.21300    2  Mg        9.88036
   6.31950      4.21300      6.31950    2  Mg        9.88036
END
```

Figure 2.23 Detail of a "feff.inp" input file of MgO with Mg as center atom for FEFF

calculation.

The suitable commands, parameter and atomic positions for FEFF-XAS spectrum calculations can be edited within the input file named "feff.inp", which is shown in Figure 2.23. This file controlled with some details, for instance the generator of input file and the number of atom which is contain in the cluster. The followed details describe about various card use to assign the steps of calculation. The type of atomic potentials and defined atomic symbols are presented in the next part, and eventually with the locations of the created atoms in the system where the location of center atom is placed at (0,0,0) in (x,y,z) coordination.

2.7.2   XAS Calculation

Calculation of XAS can be carried out with the imaginary part of one-electron Green's function operator (Ankudinov, 1998)

$$G = [E - H]^{-1},$$
(2.29)

where H is the effective one-electron operator Hamiltonian and E is the photoelectron energy. Based on the Green's-function calculation in the complex plane, to explicit equation (2.25) by using spectral representation with Green-function operator, thus the absorption coefficient can be rewritten as

$$\tilde{\mu}(E) \propto -\frac{2}{\pi} \text{Im} \langle i \,|\, \hat{\varepsilon} \cdot \vec{r}' G(\vec{r}', \vec{r}, E) \hat{\varepsilon} \cdot \vec{r} \,|\, i \rangle,$$
(2.30)

where $G(\vec{r}', \vec{r}, E) = \langle \vec{r}' \,|\, G(E + in) \,|\, \vec{r} \rangle$, $\hat{\varepsilon}$ is the x-ray polarization vector and the parameters denoted with prime is that quantity in final state (Ankudinov, 1998). Furthermore, since only the transition to unoccupied state above Fermi energy are permitted and the effect of core-hole lifetime and experimental resolution are essentially taken in to calculation, the total absorption coefficient should become

$$\mu(E) = \int\limits_{E_F}^{\infty} dE' \tilde{\mu}(E') \frac{\Gamma}{\pi[(E-E')^2 + \Gamma^2]}, \qquad (2.31)$$

where Γ is determined by the combined sum of the core-hold life time and experimental resolution, and E_F is Fermi level energy. FEFF code aid scientist to approach the XAS spectra by performing the possibly precise Green's function in $\tilde{\mu}(E)$. For FEFF 8 series, the developers suggested two mains developed feature for XAS calculation. The two main advantage are the approaches of self-consistent field (SCF) and full multiple scattering (FMS).

For XAS calculation (especially XANES), the SCF loop are used to create the SCF potentials and compute the total electron density and Coulomb potential within RSMS Green's-function framework. In FEFF 8.2 code, the SCF potentials are implemented using the spherical or "muffin-tin potential" as illustrated in Figure 2.24. Muffin-tin potential considers the atomic interval potential since a spherical scattering potential center on each atom equal to sum of overlapping potential and has a constant value in the interstitial region between atoms. FMS card will perform the calculation for all possible paths within the defined cluster.

(a)   (b)
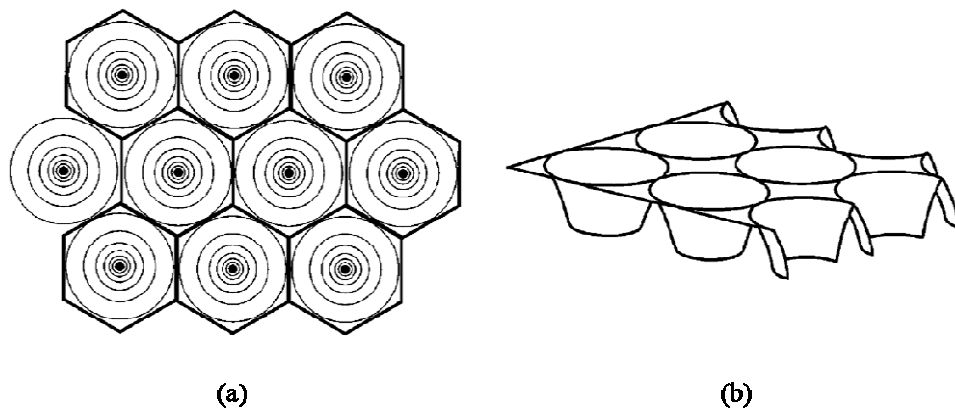
Figure 2.24 Schematic illustration of muffin-tin potential in two dimensions (Rehr and Albers, 2000).

The SCF loop constructs Green's function, which consist of central atom and scattering contribution

$$G(\vec{r},\vec{r}',E) = G^{C}(\vec{r},\vec{r}',E) + G^{SC}(\vec{r},\vec{r}',E), \tag{2.32}$$

where $G^{C}(\vec{r},\vec{r}',E)$ and $G^{SC}(\vec{r},\vec{r}',E)$ are central and scattering contribution, respectively.

XANES calculation can be performed under the defined control cards, most of them are normally used as the defaults, excepting FMS and SCF which are importantly managed. For SCF consideration, the cluster radius is used to define the suitable scattering potential, which usually requires around 30 atoms within the cluster. That cluster radius should be defined at the consistent of calculated absorption spectra as shown in Figure 2.25. The appropriate SCF cluster should be the least value that makes the consistent of the spectra presents for saving the computational resources.
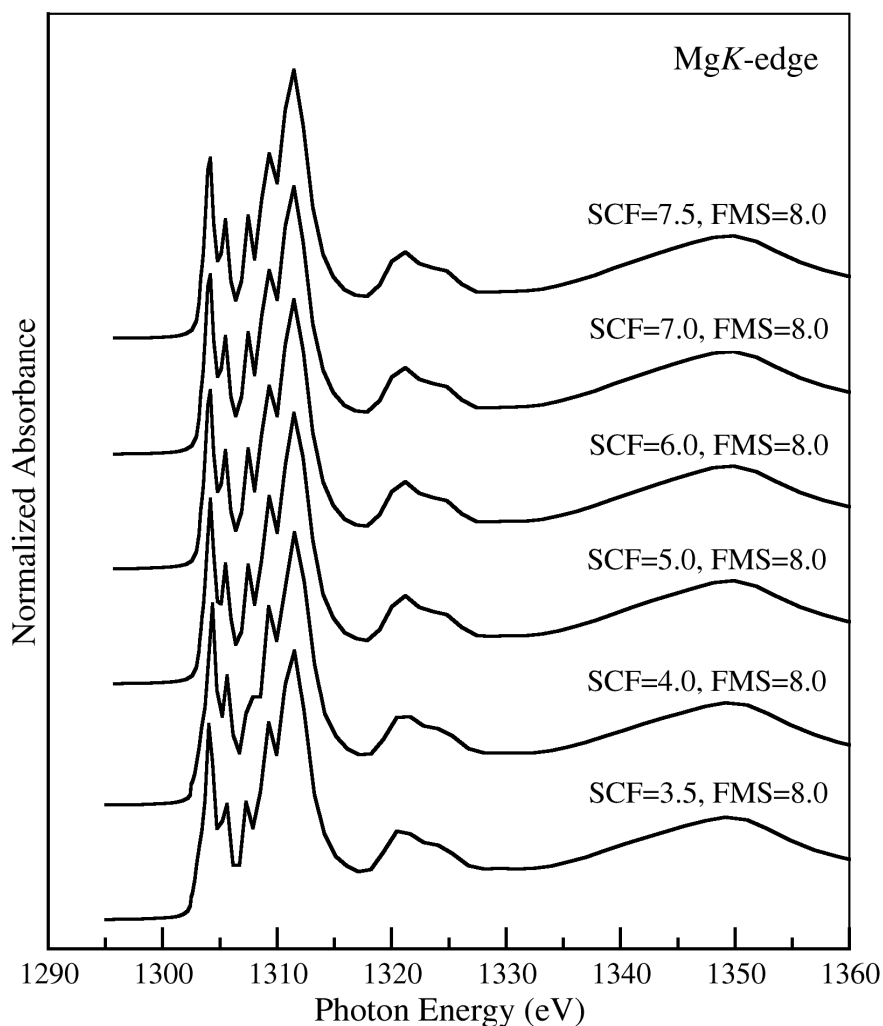
Figure 2.25 Calculated Mg K-edge XANES of MgO with different SCF parameters.

Similar to the SCF, FMS calculation should be altered gradually for the cluster radius for FMS consideration as shown in Figure 2.26. Furthermore, there are other parameters that can be changed for more satisfied spectra, such as the step size of energy.

For EXAFS calculation, the scattering muffin-tin has less effect to the calculated spectra than at the lower energy region. At EXAFS region, the photoelectron gain larger energy, and then it is less sensitive to the details of potential

between atoms. Therefore, SCF calculation may not be essential in the EXAFS

calculation.
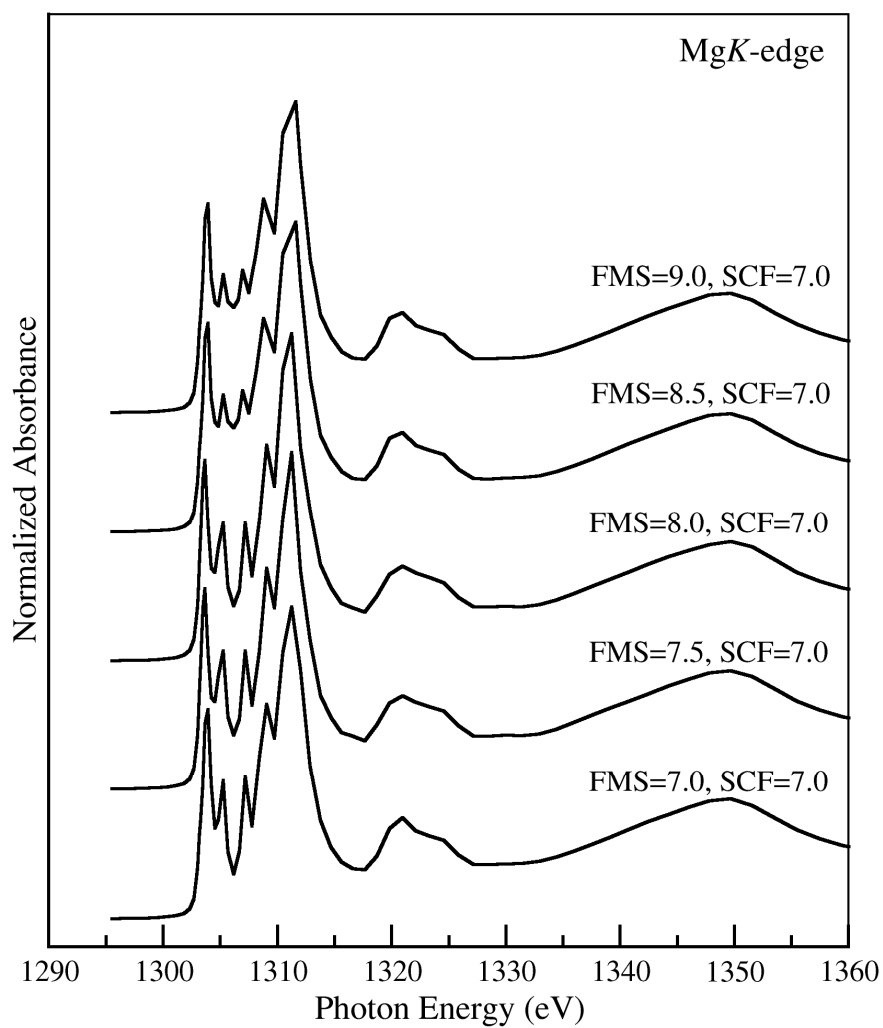
Figure 2.26 Calculated Mg K-edge XANES of MgO with different FMS parameters.

CHAPTER III

STANDARD CHARACTERIZATION

RESULTS AND DISCUSSIONS

In this chapter, the structural characterization and the interpretation of the experimental data will be presented and discussed. First, the preparation of $Mg_xZn_{1-x}O$ nanocrastals by oxalate-based co-precipitation is presented. Then characterization results by x-ray diffraction (XRD), energy dispersive spectroscopy (EDS), transmission electron microscope (TEM) images, electron diffraction and ultraviolet-visible spectroscopy will be given and discussed. The x-ray absorption spectroscopy (XAS) results, will be analyzed and presented with discussion in chapter IV.

3.1 Oxalate-based co-precipitation

In this work, the synthesis of $Mg_xZn_{1-x}O$ nanocrystals was based on chemical method called oxalate-based co-precipitation (Ertl, Knözinger, and Weitkamp, 1999). This technique is based on the different solubility of the cation in the oxalate compounds.

$Mg_xZn_{1-x}O$ nanocrystals were prepared by oxalate-based co-precipitation method. Zinc acetate dehydrate, magnesium acetate tetrahydrate and oxalic acid dehydrate were used as the starting precursors. First, we mixed aqueous solutions of zinc and magnesium acetates in oxalic acid solution in the ratio of

$[Zn^{+2}]:[Mg^{+2}]:[C_2O_4^{-2}] = (1-x):x:1.05$, the mixed oxalate precursors $Mg_xZn_{1-x}(C_2O_4)\cdot 2H_2O$ ($x = 0$, 0.01, 0.04, 0.06, 0.10, 0.15, 0.25, 0.30, 0.35, 0.50, 0.70, 0.80, 0.90) could be occurred. After that, the precipitates were washed with copious quantities of de-ionized water. Then the precipitates at each Mg concentration were dried at 60°C for 4 h and heating in air at 550°C for 24 h. Finally, the $Mg_xZn_{1-x}O$ nanocrystals were kept in a humidity controlled cabinet at room temperature before characterizations. The picture of ZnO, MgO and $Mg_xZn_{1-x}O$ nanocrystals are shown in Figure 3.1-3.3. It reveals that the colors of all the samples appear white.

(a) ZnO

(b) MgO

(c) $Mg_{0.01}Zn_{0.99}O$

(d) $Mg_{0.04}Zn_{0.96}O$

Figure 3.1 ZnO, MgO and $Mg_xZn_{1-x}O$ nanocrystals at Mg contents ($x = 0$, 1, 0.01 and 0.04).

(a) $Mg_{0.06}Zn_{0.94}O$

(b) $Mg_{0.10}Zn_{0.90}O$

(c) $Mg_{0.15}Zn_{0.85}O$

(d) $Mg_{0.25}Zn_{0.80}O$

(e) $Mg_{0.30}Zn_{0.70}O$

(f) $Mg_{0.35}Zn_{0.65}O$

(g) $Mg_{0.50}Zn_{0.50}O$

(h) $Mg_{0.70}Zn_{0.30}O$

Figure 3.2 $Mg_xZn_{1-x}O$ nanocrystals at different the contents ($x = 0.06$-0.7).

(a) $Mg_{0.80}Zn_{0.20}O$ (b) $Mg_{0.90}Zn_{0.10}O$

Figure 3.3 $Mg_xZn_{1-x}O$ nanocrystals at different the Mg contents ($x = 0.8, 0.9$)

3.2 X-ray diffraction (XRD)

The crystal structure of the $Mg_xZn_{1-x}O$ nanocrystals were characterized by the BRUKER X-ray diffractometer model D 5005, wave length 1.54 Å. The patterns of XRD for $Mg_xZn_{1-x}O$ nanocrystals at different the Mg concentration are shown in Figure 3.4.

From Figure 3.4, it can be seen that the patterns of the pure ZnO are indexed according to the known hexagonal phase (zincite), and that of MgO is indexed according to its cubic phase (periclase). Clear indications for segregation into a hexagonal and a cubic phase are found for samples having magnesium content $0.06 \leq x \leq 0.80$. Samples of $x = 0.04$ showed a very weak (200) reflection of the MgO phase, indicating that the majority of the material was in the form of zincite. At composition of $Mg_{0.90}Zn_{0.10}O$, the cubic phase was the only one seen.
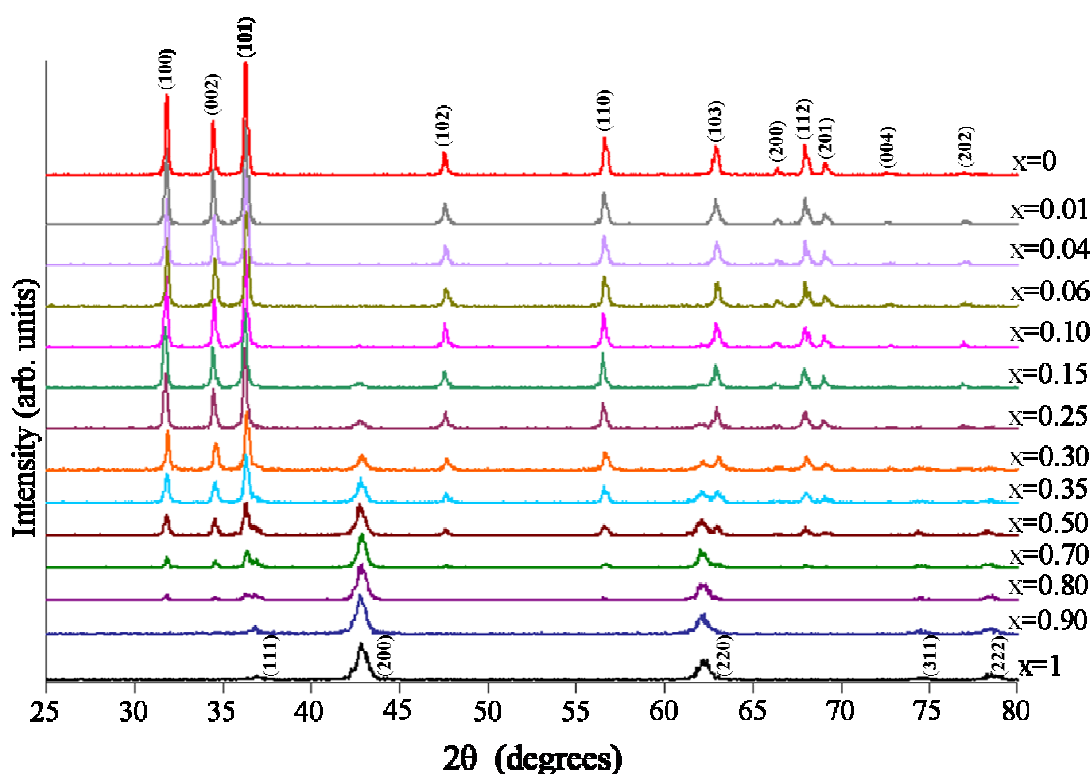
Figure 3.4 XRD patterns of Mg$_x$Zn$_{1-x}$O nanocrystals.

The appearance of the reflections in the powder patterns pertaining to two different phases indicates that particles with contrast in phase structure and elemental composition have been formed in a particular range of overall composition at the temperature and time interval of the calcination.

From full-width at half-maximum (FWHM) of the strongest diffraction peak at each the Mg concentration, the crystallite size was determined by Debye-Scherrer formula using equation 2.11. The grain sizes of products are about 15 - 60 nm which can be said that the products are nanocrystals. Notice that, the gain sizes of products tended to decrease as the Mg content increased as shown in Table 3.1. These results are confirmed by TEM measurements.

The relative percentage of the hexagonal and cubic phases of $Mg_xZn_{1-x}O$ nanocrystals can be determined by calculating the integrated strongest peak intensity or the total area under the strongest peak [(101) peak for hexagonal phase and (200) peak for cubic phase], after subtracting background noise, listed in Table 3.1.

The total area under the strongest peak can be used to calculate the phase ratio of RS to WZ in $Mg_xZn_{1-x}O$ nanocrystals. Therefore, the dependence of phase ratio of RS to WZ in $Mg_xZn_{1-x}O$ nanocrystals depending on the overall Mg content as shown in Figure 3.3. It can be seen that the phase ratio of RS to WZ in $Mg_xZn_{1-x}O$ nanocrystals increases linearly with Mg content and the structural phase transition from wurtzite structure of ZnO to rocksalt structure of MgO occur at the range of Mg contents between $0.04 < x < 0.90$. However, the diffraction angle in the x-ray diffractometer model D 5005 used in this work was not well calibrated and the instrumental broadening was not taken into account. The diffraction angles were also shifted due to some misalignment. Thus, the relationship between the Mg content and the phase ratio of RS to WZ which obtain form the XRD measurement may not be accurate the value. XAS measurement will be used to confirm this result.

Table 3.1 The crystallite size and the total area under the strongest peak of hexagonal and cubic phases of $Mg_xZn_{1-x}O$ nanocrystals at different the Mg concentration.

Mg concentration	Particle diameter (nm)	total area under (101) peak	total area under (200) peak
0	53.33	164.29	0
0.01	48.62	163.96	0
0.04	44.92	163.54	0
0.06	42.60	163.28	3.48
0.10	34.02	158.86	7.83
0.15	32.29	140.25	18.17
0.25	32.67	128.00	36.25
0.30	30.52	106.47	55.85
0.35	29.84	96.31	69.35
0.50	15.98	69.07	98.54
0.70	16.58	36.87	138.63
0.80	14.59	22.27	156.16
0.90	14.32	0	165.86
1.0	13.57	0	166.21
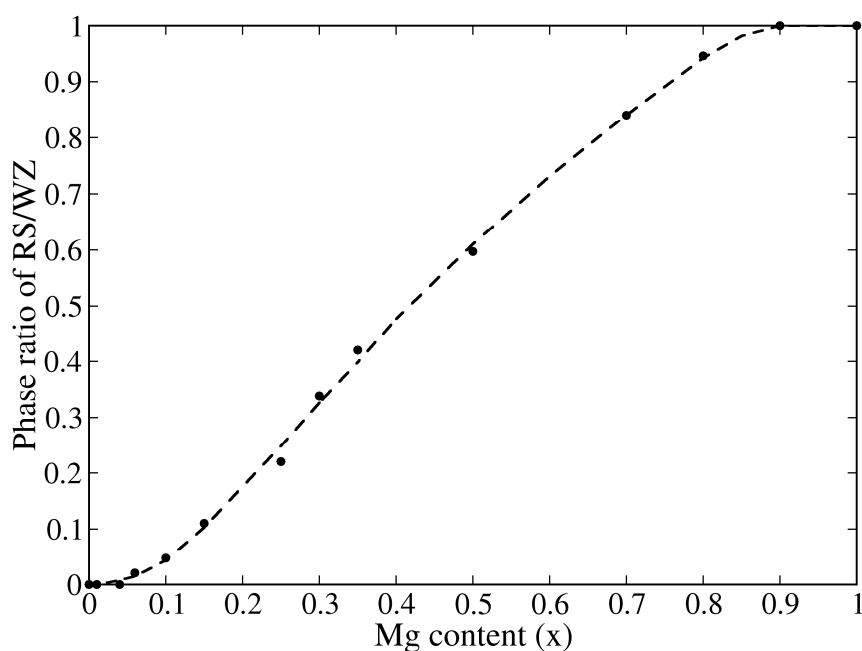
Figure 3.5 The Phase ratio of RS to WZ in $Mg_xZn_{1-x}O$ nanocrystals obtained from XRD measurement.

3.3 Energy dispersive spectroscopy (EDS)

Energy Dispersive Spectroscopy was used to analyze the composition of the synthesized products to ensure that Mg is left in $Mg_xZn_{1-x}O$ nanocrystals product. EDS spectra of the synthesized products with $x = 0.01$, 0.10 and 0.90 are shown in Figure 3.6. All peak of these spectra corresponding to elements Zn and Mg. The intensities of Mg peak increase linearly with the increase of the Mg concentration for $Mg_xZn_{1-x}O$ nanocrystals.
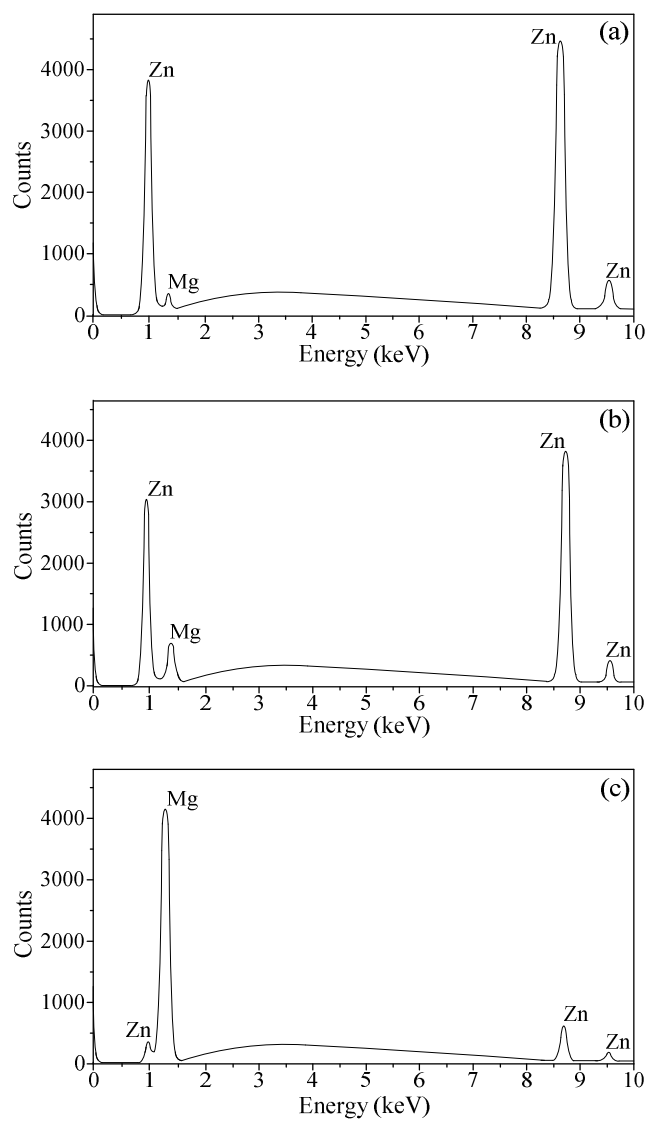
Figure 3.6 EDS spectra of (a) $Mg_{0.01}Zn_{0.99}O$ nanocrystals (b) $Mg_{0.10}Zn_{0.90}O$ nanocrystals and (c) $Mg_{0.90}Zn_{0.10}O$ nanocrystals.

3.4 Transmission electron microscope (TEM)

Transmission electron microscope was used to observe the microstructure of the synthesized products. The low-magnification image of the ZnO, MgO and $Mg_xZn_{1-x}O$ nanocrystals was illustrated in Figure 3.7 - 3.8.

(a)   (b)
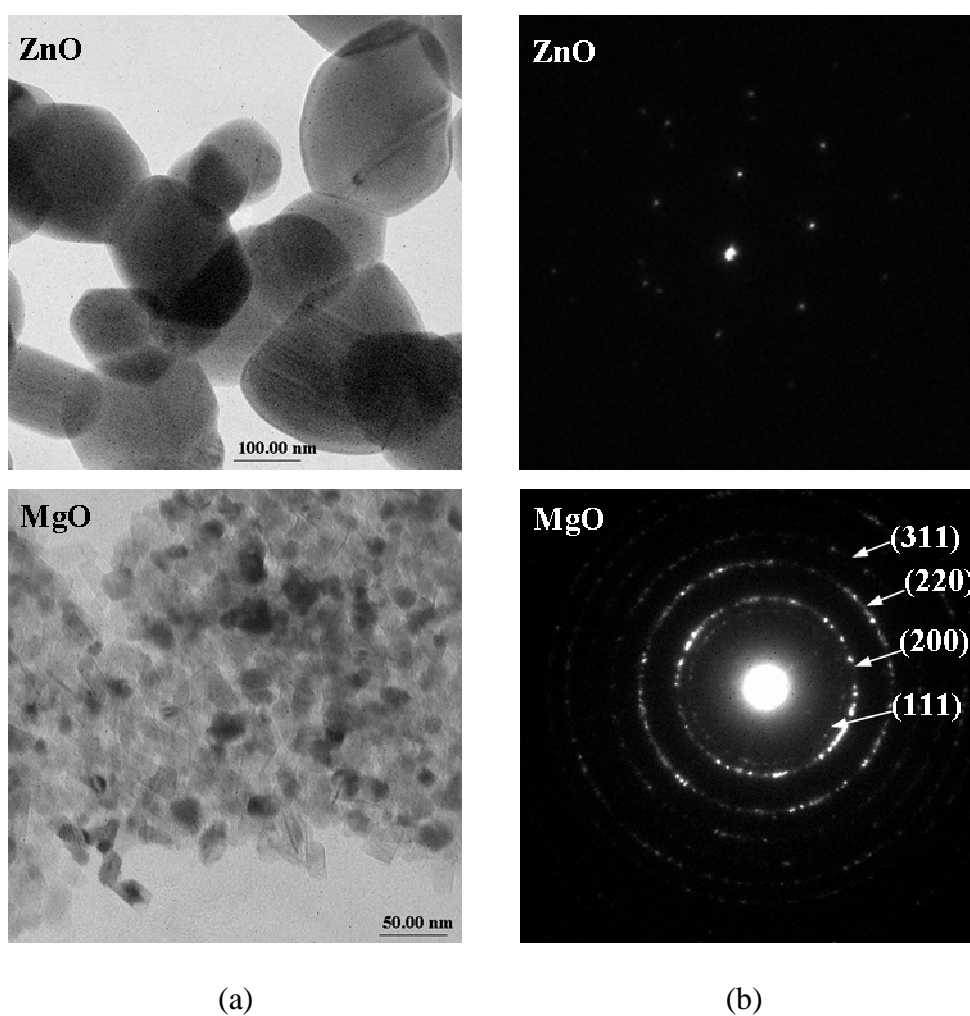
Figure 3.7 (a) TEM images of ZnO and MgO nanocrystals and (b) selected area electron diffraction patterns of ZnO and MgO nanocrystals.
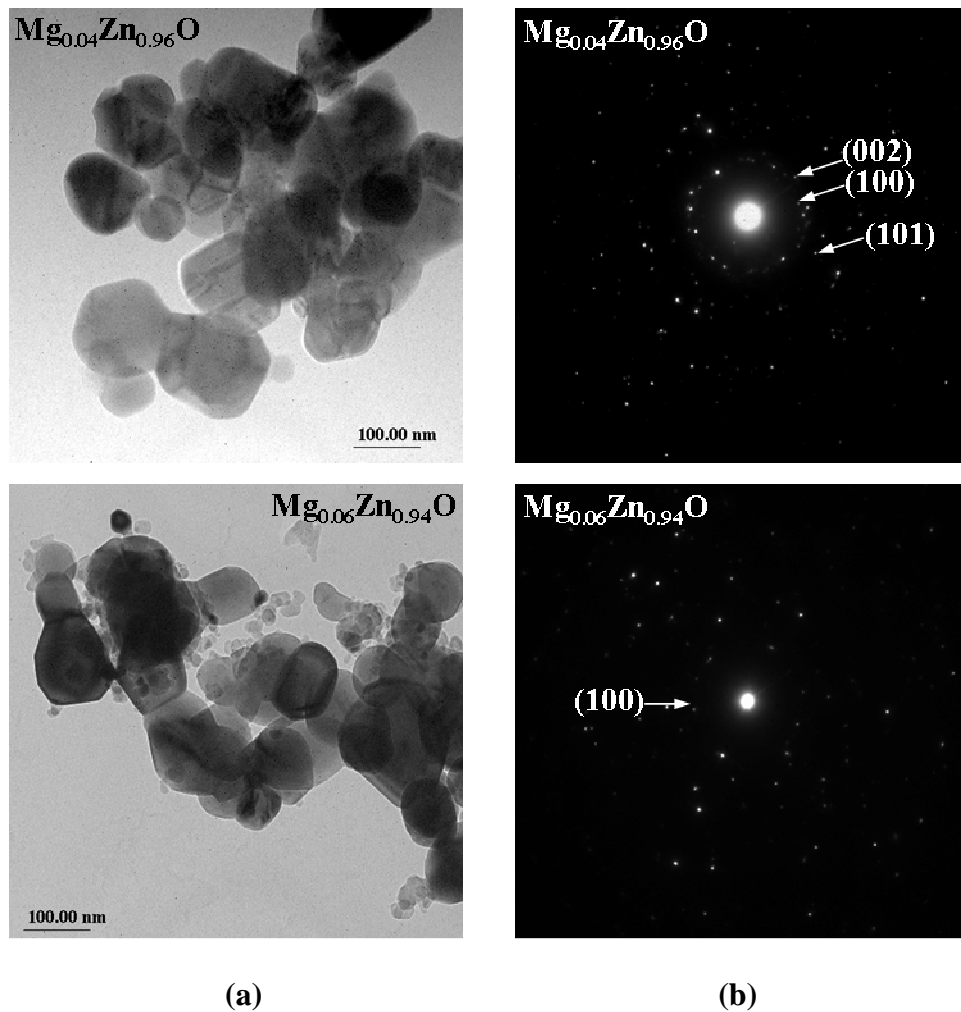
Figure 3.8 (a) TEM images of $Mg_{0.04}Zn_{0.96}O$ and $Mg_{0.06}Zn_{0.94}O$ nanocrystals and (b) selected area electron diffraction patterns of $Mg_{0.04}Zn_{0.96}O$ and $Mg_{0.06}Zn_{0.94}O$ nanocrystals.

From the TEM micrographs it can be estimated that the particle size of ZnO and MgO nanocrystals are about 80 nm and 20 nm, respectively. While TEM image of $Mg_{0.04}Zn_{0.96}O$ nanocrystals shows that the MZO nanocrystals are homogeneous and agglomerated with a particle size under 60 nm. However, when Mg concentration increased to 6%, phase separation appears in TEM image of $Mg_{0.06}Zn_{0.94}O$

nanocrystals. The particle size of $Mg_xZn_{1-x}O$ nanocrystals tended to decrease as the Mg concentration increased. These observations are consistent with the XRD result. The corresponding selected area electron diffraction (SEAD) patterns are shown in Figure 3.8 - 3.9. The index of the polycrystalline ring observed by SEAD a calibration with Si crystal has been done. The SEAD pattern of ZnO nanocrystals displays the pattern of hexagonal structure. While the SEAD pattern of MgO nanocrystals reveal the ring diffraction patterns which are in agreement with XRD results. The indexed rings of SEAD pattern of $Mg_{0.04}Zn_{0.96}O$ and $Mg_{0.06}Zn_{0.94}O$ nanocrystals agree well with XRD pattern of wurtzite ZnO. It indicates that they form the hexagonal single phase.

3.5   Ultraviolet Visible Spectroscopy (UV-VIS)

The UV-Vis spectra were collected at the Nanocomposite Material Research Laboratory, College of KMITL Nanotechnology, King Mongkult's Institute of Technology Ladkrabang. The UV-Vis measurement was performed in absorption mode. The spectra were scanned from wavelength between 200 nm to 600 nm which cover the ultraviolet and visible regions.

The UV-Vis absorption spectra of $Mg_xZn_{1-x}O$ nanocrystals are shown in Figure 3.9. It reveals that the absorption edge of pure ZnO nanocrystals was about 375 nm, while that of $Mg_{0.25}Zn_{0.75}O$ is blue-shifted to about 347 nm.
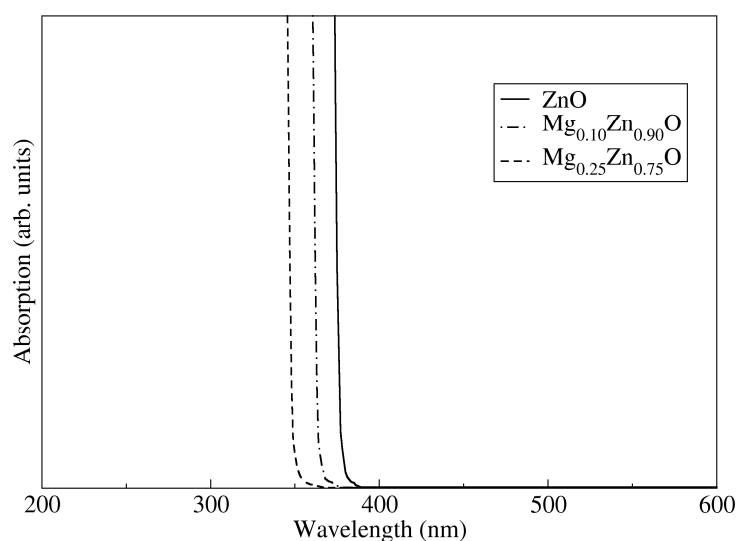
Figure 3.9 UV-visible absorption spectra of $Mg_xZn_{1-x}O$ nanocrystals

Table 3.2 The absorption edge of the UV-Vis absorption spectra and the bandgap of ZnO and $Mg_xZn_{1-x}O$ nanocrystals.

Samples	Absorption edge (nm)	Bandgap (eV)
ZnO	375	3.31
$Mg_{0.10}Zn_{0.90}O$	362	3.43
$Mg_{0.25}Zn_{0.75}O$	347	3.57

From the absorption edge of these spectra, the bandgap was determined by using equation 2.25. It clearly demonstrates that the bandgap of $Mg_xZn_{1-x}O$ nanocrystals increase as the Mg content increased, as listed in Table 3.2. This result is consistent with the research of X. Qiu *et al.* (X. Qiu *et al.*, 2008) which study about the enhanced photocatalytic activities of semiconductors, a case study of ZnO doped with Mg^{2+}.

CHAPTER IV

XAS STUDY OF MAGNESIUM ZINC OXIDE

NANOCRYSTALS

In the last chapter the microstructural study of $Mg_xZn_{1-x}O$ nanocrystals using XRD, EDS and TEM suggest that the structural phase transition from wurtzite structure of ZnO to rocksalt structure of MgO appear at the range of Mg contents between 0.04 - 0.9 and the percentage of cubic phase of $Mg_xZn_{1-x}O$ nanocrystals increases linearly with Mg content. However, the standard characterization which used in chapter III can not reveal the local structure of Mg and Zn atoms in the nanocrystals, since the mixing of WZ/RS MZO nanocrystal is not solely the phase separation between ZnO and MgO pure compounds, but the mixture of both WZ and RS, MZO nanocrystals with various compositions. Luckily, the synchrotron-based XAS facility was accessible to us through the user beamtime allocated by SLRI. It will be shown in this chapter that XAS is a powerful tool for resolving the local structure surrounding Mg atoms in $Mg_xZn_{1-x}O$ nanocrystals.

4.1 XAS measurement of $Mg_xZn_{1-x}O$ nanocrystals

XAS spectra were obtained at the XAS facility (BL-8) of the Siam Photon Laboratory, Synchrotron Light Research Institute, Nakhon Ratchasima, with the storage ring running at 1.2 GeV and beam current of 80 - 120 mA during the

measurement. XAS measurement was performed in the fluorescence mode using KTP (011) and Ge (220) monochromators for Mg K-edge and Zn K-edge XAS spectra, respectively. The x-ray transparent Kapton® tape was used to mount the samples. The spectra were collected for the K-edges of Mg (1303 eV) and Zn (9659 eV) in nanocrystal samples. XANES and EXAFS were collected at an energy step of 0.25 eV and 1.0 eV, respectively.

4.2 XANES Analysis

XANES contains the basic information about the local structure around the specific absorbing atoms. The measured Zn and Mg K-edge XANES spectra of $Mg_xZn_{1-x}O$ nanocrystals are shown in Figure 4.1 and 4.2, respectively, in comparison with ZnO and MgO spectra.

From XANES of Zn K-edge finger print, it can be seen that the feature of the spectra taken from samples with high Mg content are clearly difference from that of pure ZnO. Similarly, XANES Mg K-edge reveals that the feature of the spectra taken from samples with low Mg content ($x \leq 0.10$) are clearly difference from that of pure MgO. Therefore, two assumptions can be made from XANES measurements. First, assumption Zn resides in Mg site of RS structure in high-x samples. Second, Mg replaces Zn in the WZ low-x $Mg_xZn_{1-x}O$ samples. The XANES calculation can be used to verify these assumptions.
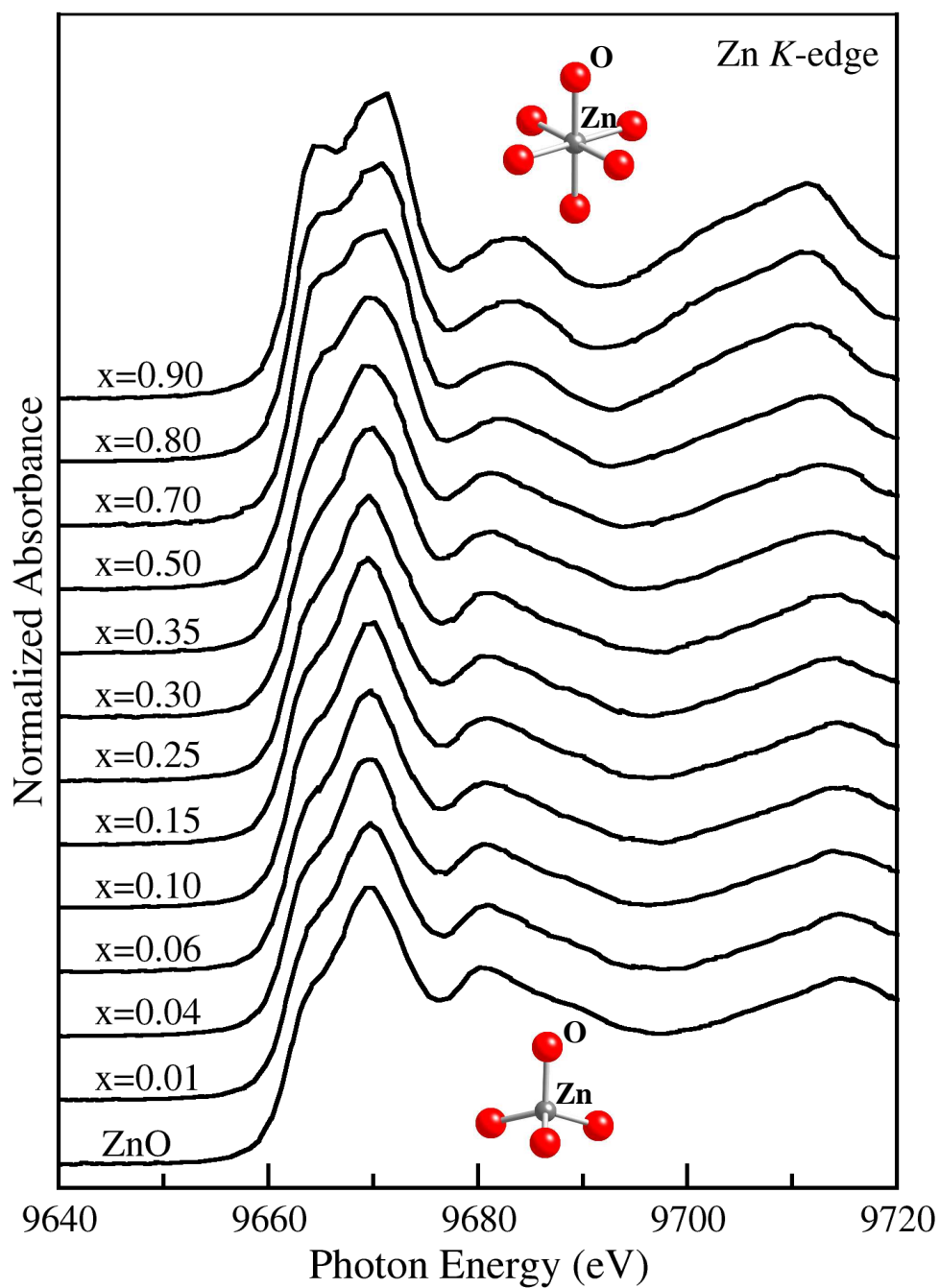
Figure 4.1 Zn *K*-edge XANES spectra of Mg$_x$Zn$_{1-x}$O nanocrystals at different the Mg

contents compared with ZnO.
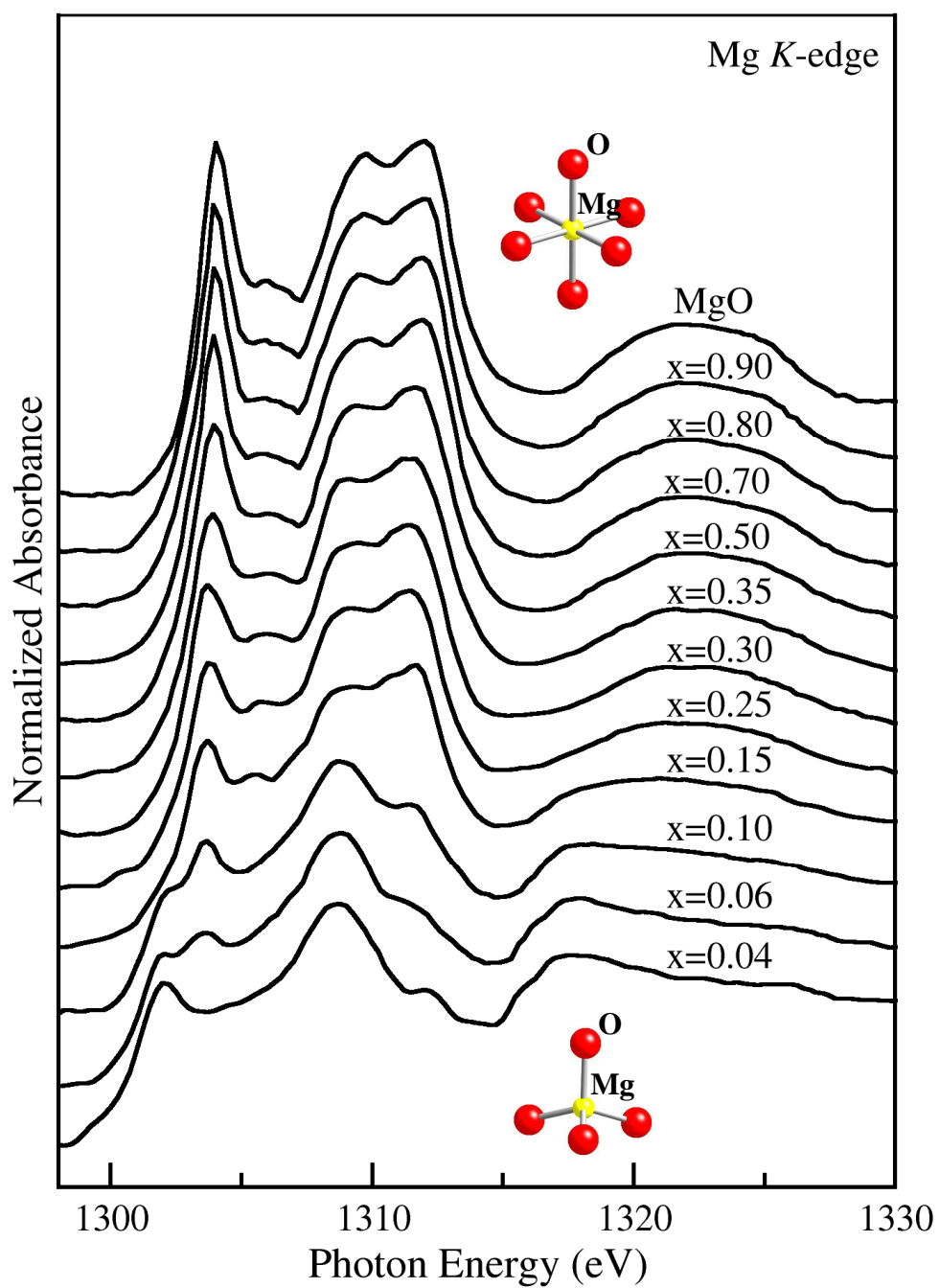
Figure 4.2 Mg *K*-edge XANES spectra of Mg$_x$Zn$_{1-x}$O nanocrystals at different the Mg contents compared with MgO.

The feature of the measured XANES spectra slowly changes as Mg contents increased. This change associated with the phase ratio of RS to WZ in $Mg_xZn_{1-x}O$ nanocrystals. RS and WZ are the most common phases of $Mg_xZn_{1-x}O$ nanocrystals. The relative proportion of RS and WZ phases in $Mg_xZn_{1-x}O$ nanocrystals can be calculated from the normalized absorbance of the measured XANES spectra of difference Mg contents. For the measured Zn K-edge XANES spectra, the normalized absorbance at photon energy 9665, 9670, 9680, 9690, and 9710 eV has been selected and shown in Table 4.1. While the normalized absorbance at photon energy 1304, 1310, 1312, 1317, and 1327 eV has been chosen for the measured Mg K-edge XANES spectra and shown in Table 4.2.

From the XRD results, ZnO and $Mg_{0.04}Zn_{0.96}O$ have a single phase of WZ while MgO and $Mg_{0.90}Zn_{0.10}O$ have a single phase of RS. Therefore, the phase ratio of RS to WZ obtained from the normalized absorbance of the measured Zn and Mg K-edge XANES spectra at different photon energy are shown in Table 4.3 and Table 4.4, respectively, and shown as a function of Mg contents in Figure 4.3 and Figure 4.4, respectively. The phase ratio of RS to WZ is allowed to vary between 0 (completely WZ) and 1 (completely RS).

Figure 4.4 and Figure 4.5 show the average phase ratio of RS to WZ in $Mg_xZn_{1-x}O$ nanocrystals as a function Mg contents, which obtained by averaging the phase ratio of RS to WZ from every the photon energy in Figure 4.3 and Figure 4.4, respectively. The average phase ratio of RS to WZ in $Mg_xZn_{1-x}O$ nanocrystals are listed in Table 4.5 and Table 4.6 for the measured Zn and Mg K-edge XANES spectra, respectively.

The average phase ratio of RS to WZ in $Mg_xZn_{1-x}O$ nanocrystals obtained from both the measured Zn and Mg K-edge XANES spectra is shown in Figure 4.7. It can be seen that the phase ratio of RS to WZ obtained from the measured Mg K-edge XANES spectra rises before that of the measured Zn K-edge XANES spectra at the low-x region and *vice versa* at the high-x region. The results demonstrated that Zn atoms occupy favorable 4-fold cation sites (WZ) more than 6-fold cation sites (RS) in high-x $Mg_xZn_{1-x}O$ nanocrystals and Mg atoms occupy favorable 6-fold cation sites (RS) more than 4-fold cation sites (WZ) in low-x $Mg_xZn_{1-x}O$ nanocrystals. No intermediate phase is needed to obtain a good fit to the XAS.

We conclude that XAS measurement technique can be applied to determine the phase ratio of RS to WZ in $Mg_xZn_{1-x}O$ nanocrystals which is impracticable by standard characterizations technique such as XRD or TEM.

Table 4.1 The normalized absorbance of the measured Zn K-edge MZO XANES spectra at different photon energies.

Samples	Normalized absorbance				
	9665	9670	9680	9690	9710
ZnO	1.170	1.720	1.215	0.965	1.030
$Mg_{0.01}Zn_{0.99}O$	1.171	1.720	1.215	0.965	1.031
$Mg_{0.04}Zn_{0.96}O$	1.172	1.722	1.213	0.963	1.032
$Mg_{0.06}Zn_{0.94}O$	1.175	1.724	1.211	0.961	1.034
$Mg_{0.10}Zn_{0.90}O$	1.178	1.726	1.204	0.957	1.038
$Mg_{0.15}Zn_{0.85}O$	1.193	1.735	1.192	0.953	1.050
$Mg_{0.25}Zn_{0.75}O$	1.240	1.754	1.163	0.930	1.080
$Mg_{0.30}Zn_{0.70}O$	1.279	1.765	1.142	0.918	1.100
$Mg_{0.35}Zn_{0.65}O$	1.312	1.776	1.120	0.896	1.121
$Mg_{0.50}Zn_{0.50}O$	1.401	1.807	1.056	0.835	1.175
$Mg_{0.70}Zn_{0.30}O$	1.505	1.841	0.964	0.766	1.248
$Mg_{0.80}Zn_{0.20}O$	1.546	1.856	0.928	0.727	1.281
$Mg_{0.90}Zn_{0.10}O$	1.572	1.865	0.900	0.710	1.302

Table 4.2 The normalized absorbance of the measured Mg K-edge MZO XANES spectra at different photon energies.

Samples	Normalized absorbance				
	1304	1310	1312	1317	1327
$Mg_{0.04}Zn_{0.96}O$	0.980	1.520	1.100	1.318	1.070
$Mg_{0.06}Zn_{0.94}O$	1.000	1.536	1.130	1.312	1.068
$Mg_{0.10}Zn_{0.90}O$	1.080	1.582	1.200	1.300	1.062
$Mg_{0.15}Zn_{0.85}O$	1.320	1.680	1.330	1.240	1.047
$Mg_{0.25}Zn_{0.75}O$	1.560	1.930	1.700	1.130	1.012
$Mg_{0.30}Zn_{0.70}O$	1.700	2.020	1.880	1.080	0.992
$Mg_{0.35}Zn_{0.65}O$	1.800	2.100	2.020	1.040	0.974
$Mg_{0.50}Zn_{0.50}O$	2.080	2.230	2.280	0.920	0.932
$Mg_{0.70}Zn_{0.30}O$	2.330	2.310	2.430	0.806	0.885
$Mg_{0.80}Zn_{0.20}O$	2.400	2.350	2.500	0.760	0.866
$Mg_{0.90}Zn_{0.10}O$	2.460	2.372	2.530	0.745	0.857
MgO	2.480	2.380	2.540	0.736	0.854

Table 4.3 The phase ratio of RS to WZ obtained from the measured Zn K-edge MZO

XANES spectra at different photon energies.

Mg contents	Phase ratio of RS to WZ				
	9665	9670	9680	9690	9710
0.00	0.000	0.000	1.000	1.000	0.000
0.01	0.002	0.000	1.000	1.000	0.004
0.04	0.005	0.014	0.994	0.992	0.007
0.06	0.012	0.041	0.987	0.984	0.015
0.10	0.020	0.041	0.965	0.973	0.029
0.15	0.057	0.103	0.927	0.945	0.074
0.25	0.174	0.234	0.835	0.863	0.184
0.30	0.271	0.310	0.768	0.816	0.257
0.35	0.353	0.386	0.689	0.729	0.335
0.50	0.575	0.600	0.495	0.490	0.553
0.70	0.833	0.934	0.203	0.220	0.801
0.80	0.935	0.938	0.089	0.086	0.923
0.90	1.000	1.000	0.000	0.000	1.000

Table 4.4 The phase ratio of RS to WZ obtained from the measured Mg K-edge MZO

XANES spectra at different photon energies.

Mg contents	Phase ratio of RS to WZ				
	1304	1310	1312	1317	1327
0.04	0.000	0.000	0.000	1.000	1.000
0.06	0.010	0.019	0.021	0.990	0.991
0.10	0.040	0.072	0.069	0.969	0.963
0.15	0.160	0.186	0.160	0.866	0.894
0.25	0.387	0.477	0.417	0.677	0.731
0.30	0.480	0.581	0.542	0.591	0.639
0.35	0.547	0.674	0.639	0.522	0.556
0.50	0.733	0.826	0.819	0.316	0.361
0.70	0.900	0.919	0.924	0.120	0.144
0.80	0.947	0.965	0.965	0.041	0.056
0.90	0.987	0.991	0.993	0.007	0.014
1.00	1.000	1.000	1.000	0.000	0.000
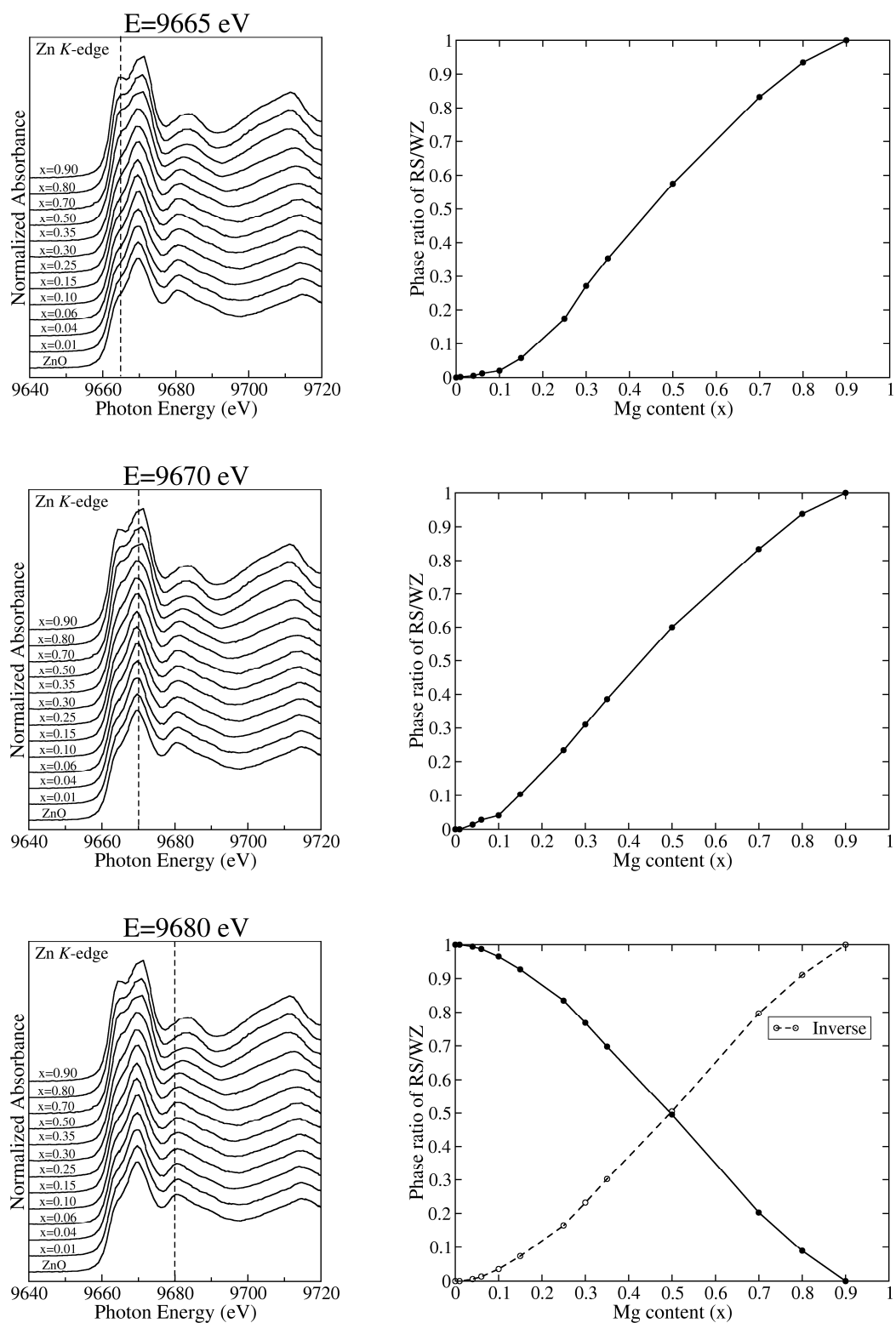
Figure 4.3 The phase ratio of RS to WZ obtained from the measured Zn *K*-edge

XANES spectra at different photon energies as a function of Mg contents.
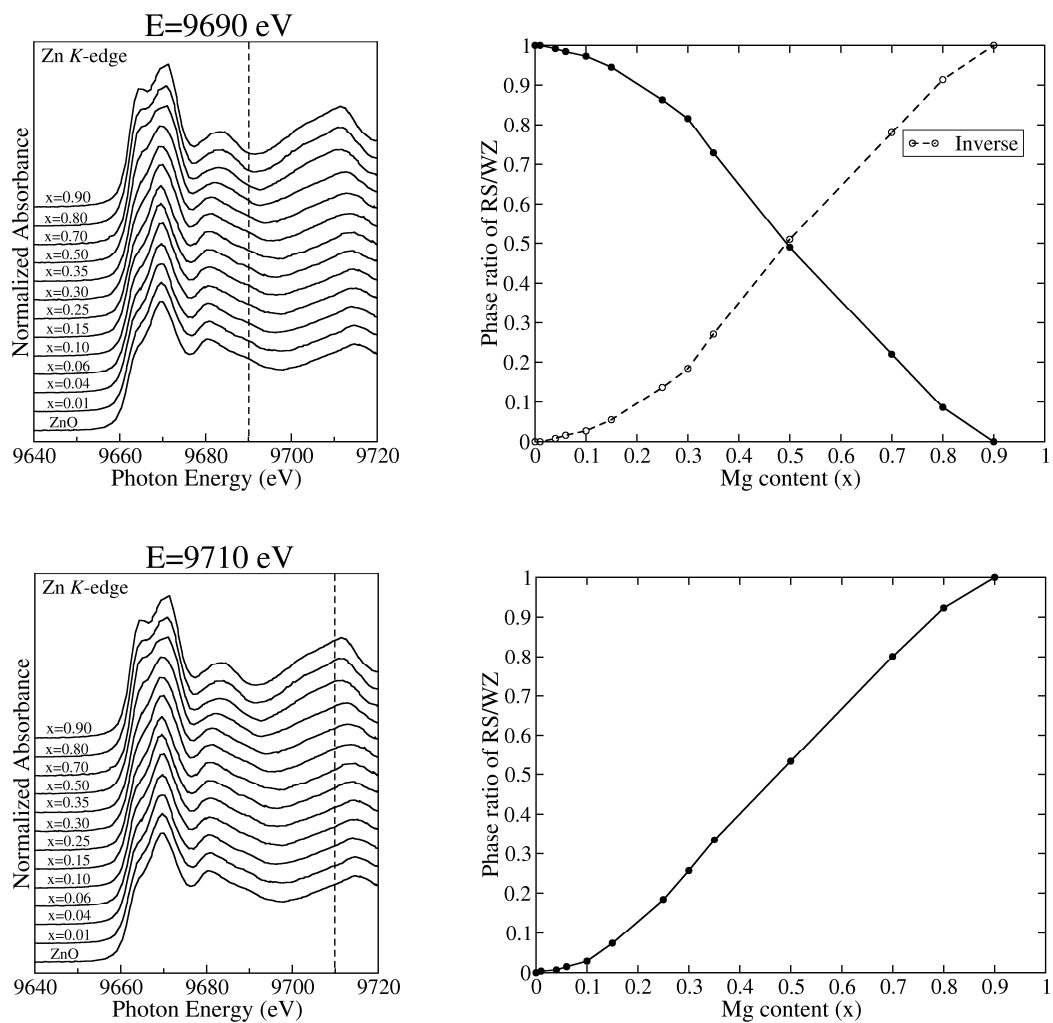
Figure 4.3 (Continued).
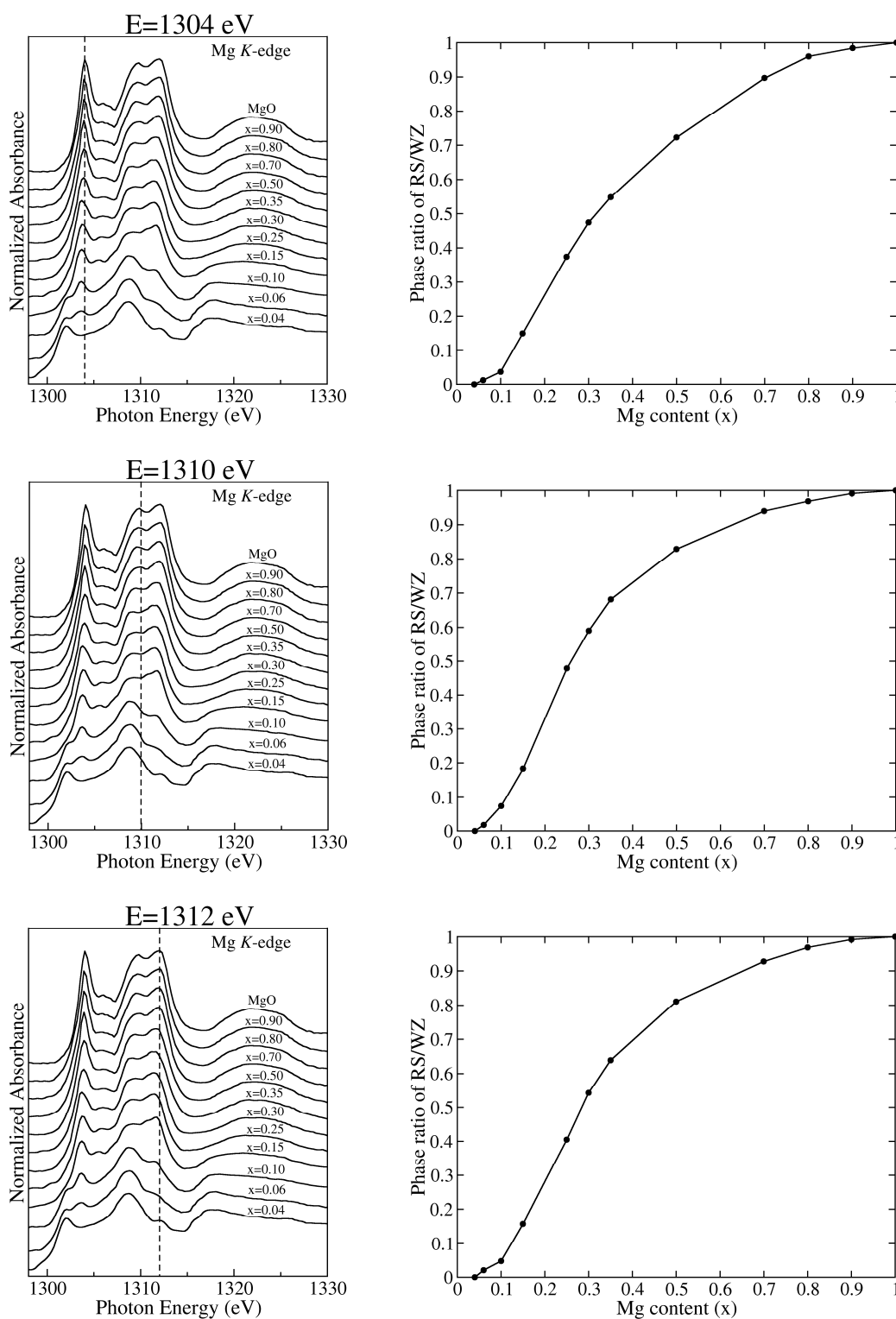
Figure 4.4 The phase ratio of RS to WZ obtained from the measured Mg *K*-edge

XANES spectra at different photon energies as a function of Mg contents.
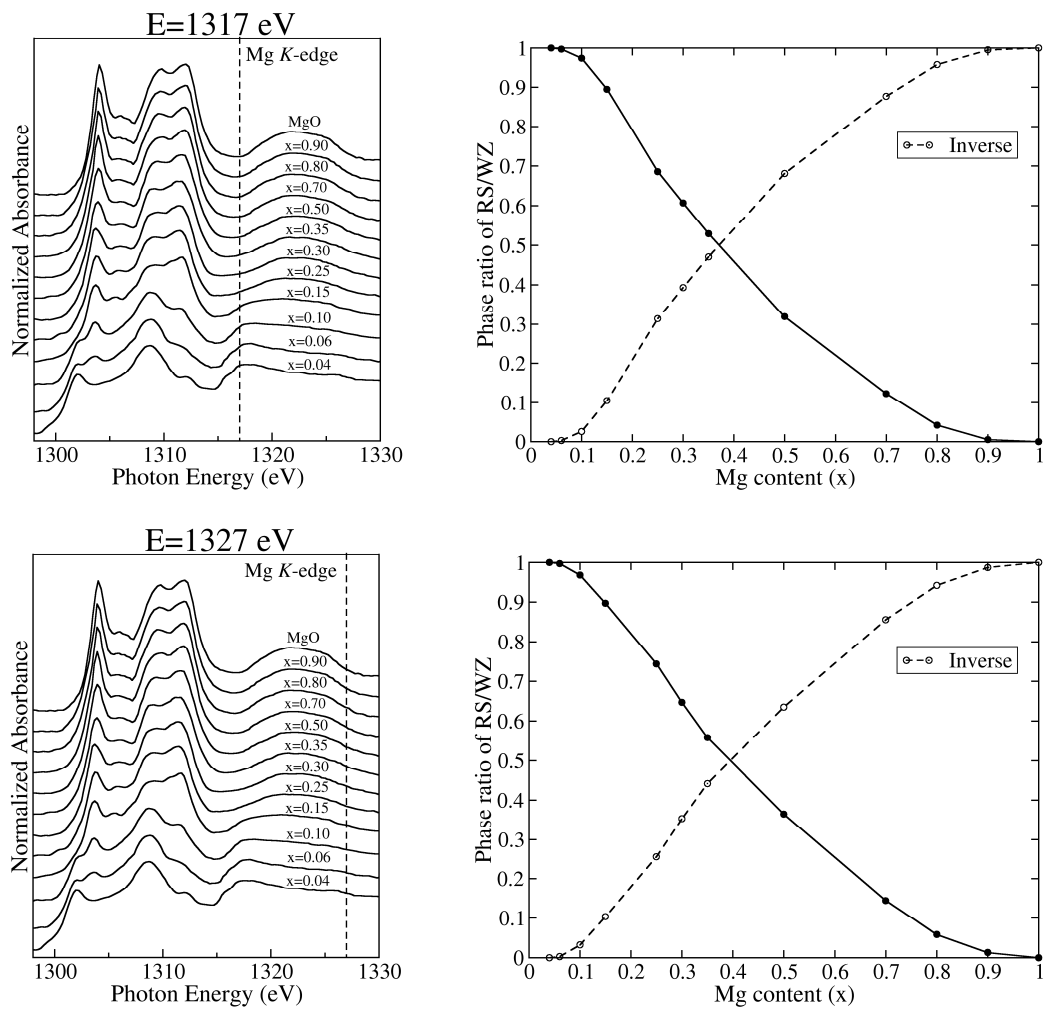
Figure 4.4 (Continued).

Figure 4.5 The average phase ratio of RS to WZ in Mg$_x$Zn$_{1-x}$O nanocrystals obtained from the measured Zn K-edge XANES spectra as a function of Mg contents.

Figure 4.6 The average phase ratio of RS to WZ in Mg$_x$Zn$_{1-x}$O nanocrystals obtained from the measured Mg K-edge XANES spectra as a function of Mg contents.

Table 4.5 The average phase ratio of RS and WZ in $Mg_xZn_{1-x}O$ nanocrystals obtained from the measured Zn K-edge XANES spectra.

Samples	Ratio of RS phase	Ratio of WZ phase
ZnO	0.000	1.000
$Mg_{0.01}Zn_{0.99}O$	0.001	0.999
$Mg_{0.04}Zn_{0.96}O$	0.008	0.992
$Mg_{0.06}Zn_{0.94}O$	0.017	0.983
$Mg_{0.10}Zn_{0.90}O$	0.031	0.969
$Mg_{0.15}Zn_{0.85}O$	0.072	0.928
$Mg_{0.25}Zn_{0.75}O$	0.179	0.821
$Mg_{0.30}Zn_{0.70}O$	0.251	0.749
$Mg_{0.35}Zn_{0.65}O$	0.329	0.671
$Mg_{0.50}Zn_{0.50}O$	0.544	0.456
$Mg_{0.70}Zn_{0.30}O$	0.809	0.191
$Mg_{0.80}Zn_{0.20}O$	0.924	0.076
$Mg_{0.90}Zn_{0.10}O$	1.000	0.000

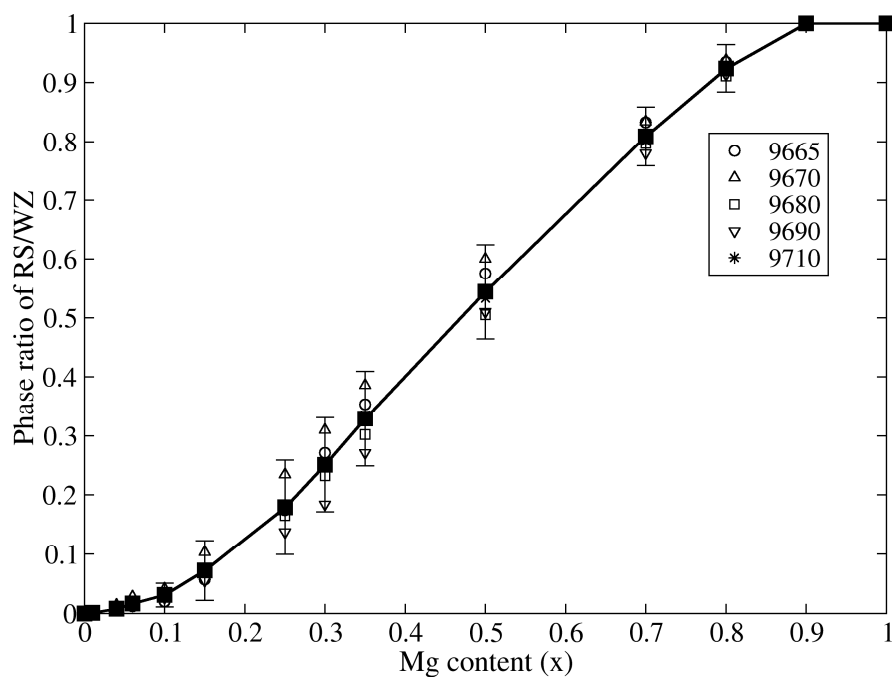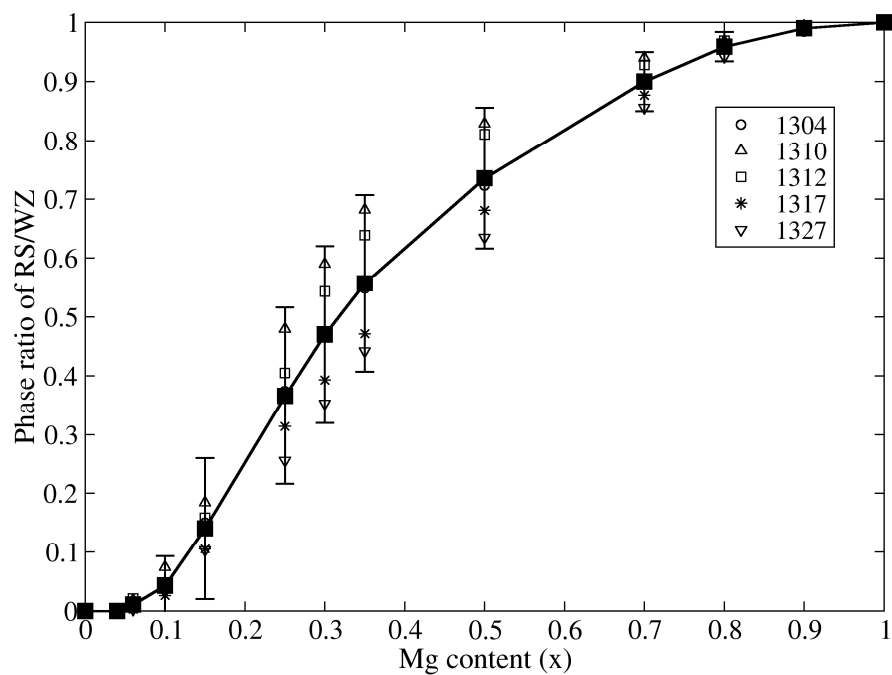**Table 4.6** The average phase ratio of RS and WZ in $Mg_xZn_{1-x}O$ nanocrystals obtained from the measured Mg K-edge XANES spectra.

Samples	Ratio of RS phase	Ratio of WZ phase
$Mg_{0.04}Zn_{0.96}O$	0.000	1.000
$Mg_{0.06}Zn_{0.94}O$	0.011	0.986
$Mg_{0.10}Zn_{0.90}O$	0.050	0.950
$Mg_{0.15}Zn_{0.85}O$	0.149	0.851
$Mg_{0.25}Zn_{0.75}O$	0.374	0.626
$Mg_{0.30}Zn_{0.70}O$	0.475	0.525
$Mg_{0.35}Zn_{0.65}O$	0.556	0.444
$Mg_{0.50}Zn_{0.50}O$	0.740	0.260
$Mg_{0.70}Zn_{0.30}O$	0.896	0.104
$Mg_{0.80}Zn_{0.20}O$	0.966	0.034
$Mg_{0.90}Zn_{0.10}O$	0.991	0.009
MgO	1.000	0.000
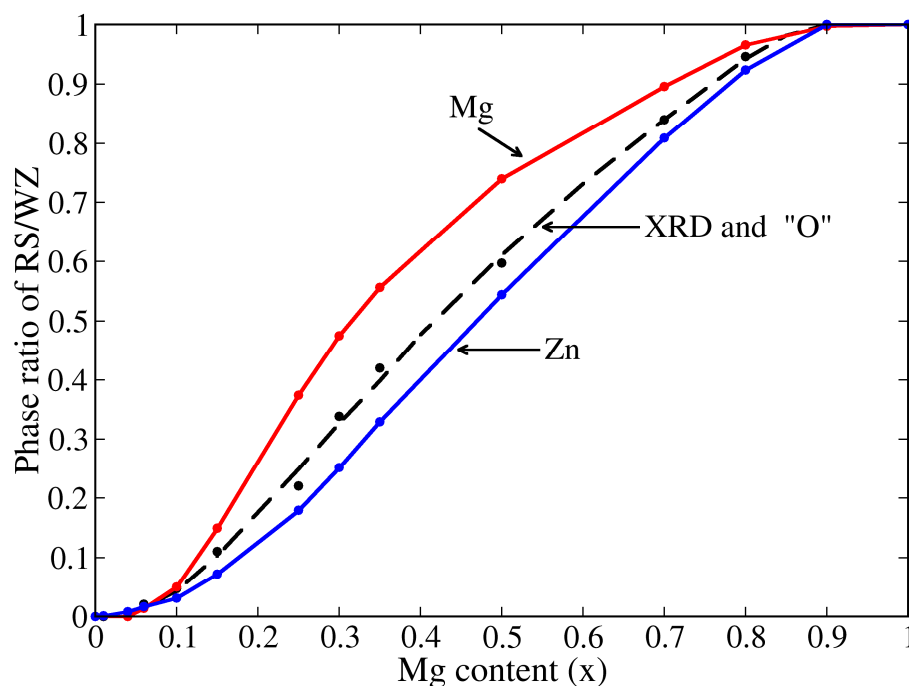
Figure 4.7 Comparison of the average phase ratio of RS to WZ in $Mg_xZn_{1-x}O$ nanocrystals obtained from the measured Zn (blue line) and Mg (red line) K-edge XANES spectra. The phase ratio of RS to WZ obtained from XRD measurement is shown in dash line. <u>This is an evidence that Mg prefers 6-fold site more than Zn and Zn prefers 4-fold site more than Mg in MZO nanocrystals at any composition</u>.

4.3 Calculation of X-ray absorption spectroscopy

FEFF 8.2 code is used to calculate XANES spectra of ZnO, Zn in MgO, MgO and Mg in ZnO. After generate "feff.inp", there are some input parameters needed. For wurtzite MZO, the lattice parameters a=3.2427 Å and c=5.1948 Å (Decremps *et al.*, 2003) are used. For rocksalt MZO, the parameter a=4.213 Å (Oganov *et al.*, 2003) is used in the calculation. We found that variations of metal-oxygen bond lengths for several percent do not change the spectra features noticeably, therefore the lattice distortion was not considered in XANES calculations. For Zn K-edge calculation, a cluster of 42 atoms (radius of 5.0 Å) is used to calculate the self-consistent field

muffin-tin atomic potentials within the Hedin-Lundqvist exchange potential. After the potentials are obtained, a 144-atom cluster (radius of 7.5 Å) is used for the full multiple scattering calculation. The self-consistent calculations are performed in the sphere radius 7 Å (~ 170 atoms) around the absorber Mg atom. The full multiple scattering calculations include all possible paths within a larger cluster radius of 8.5 Å (~ 257 atoms). Zn in MgO model was created by using MgO rocksalt framework and replaces the absorber Mg atom with Zn. While using ZnO wurtzite framework for Mg in ZnO model and substitute the absorber Zn atom with Mg. The larger cluster provided no need to introduce Z+1 scheme as suggested recently in the literature for Mg *K*-edge XANES simulation.

The calculated Zn and Mg *K*-edge XANES spectra of MZO with various composition can be simulated by using linear combination of the phase ratio of RS to WZ from Table 4.5 and Table 4.6, respectively. The results of the calculated linear combination Zn and Mg *K*-edge XANES spectra are compared with the measured Zn and Mg *K*-edge XANES spectra of $Mg_xZn_{1-x}O$ nanocrystals, as shown in Figure 4.8 and Figure 4.9, respectively. It can be seen that, the calculated linear combination XANES spectra give features that can be matched with the experimental spectra. This result confirms that Zn atoms occupy 6-fold cation sites in RS $Mg_xZn_{1-x}O$ and Mg atoms occupy 4-fold cation sites in WZ $Mg_xZn_{1-x}O$.

Figure 4.8 (a) The measured Zn *K*-edge XANES spectra of $Mg_x Zn_{1-x}O$ nanocrystals, and (b) the calculated Zn K-edge XANES spectra from linear combination of ZnO and Zn in MgO with various proportions.
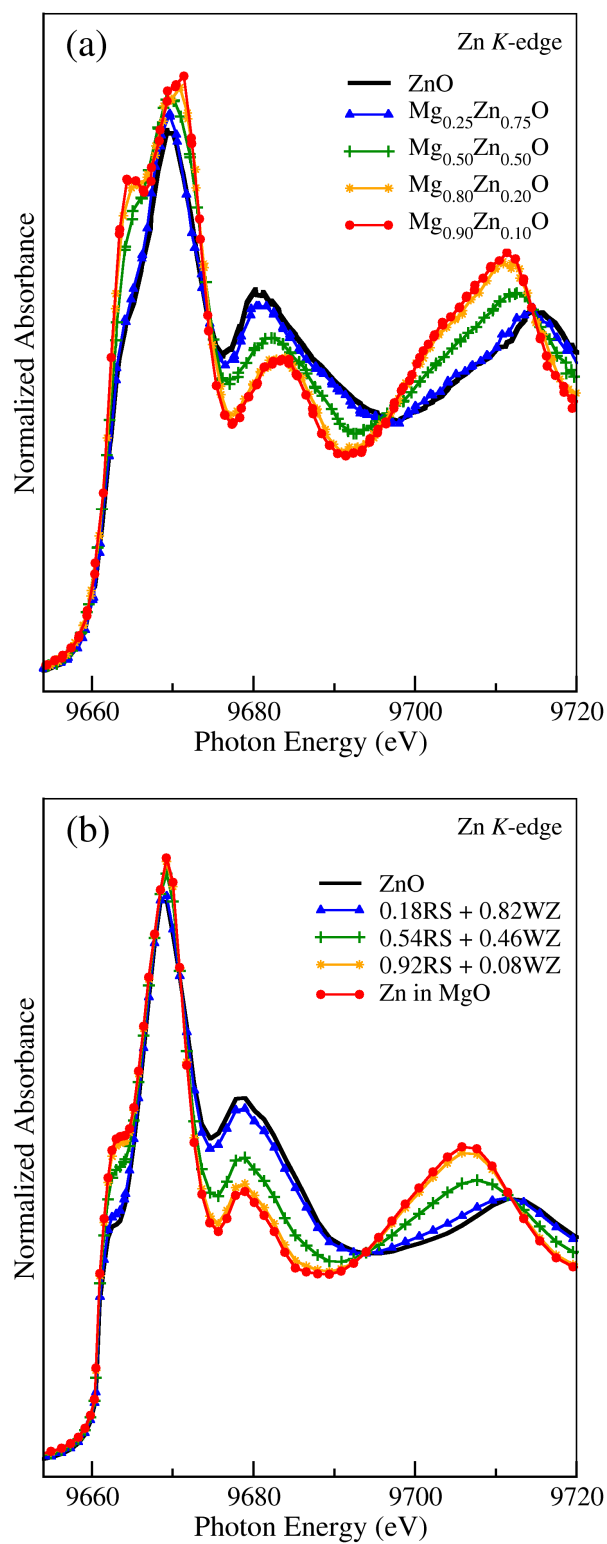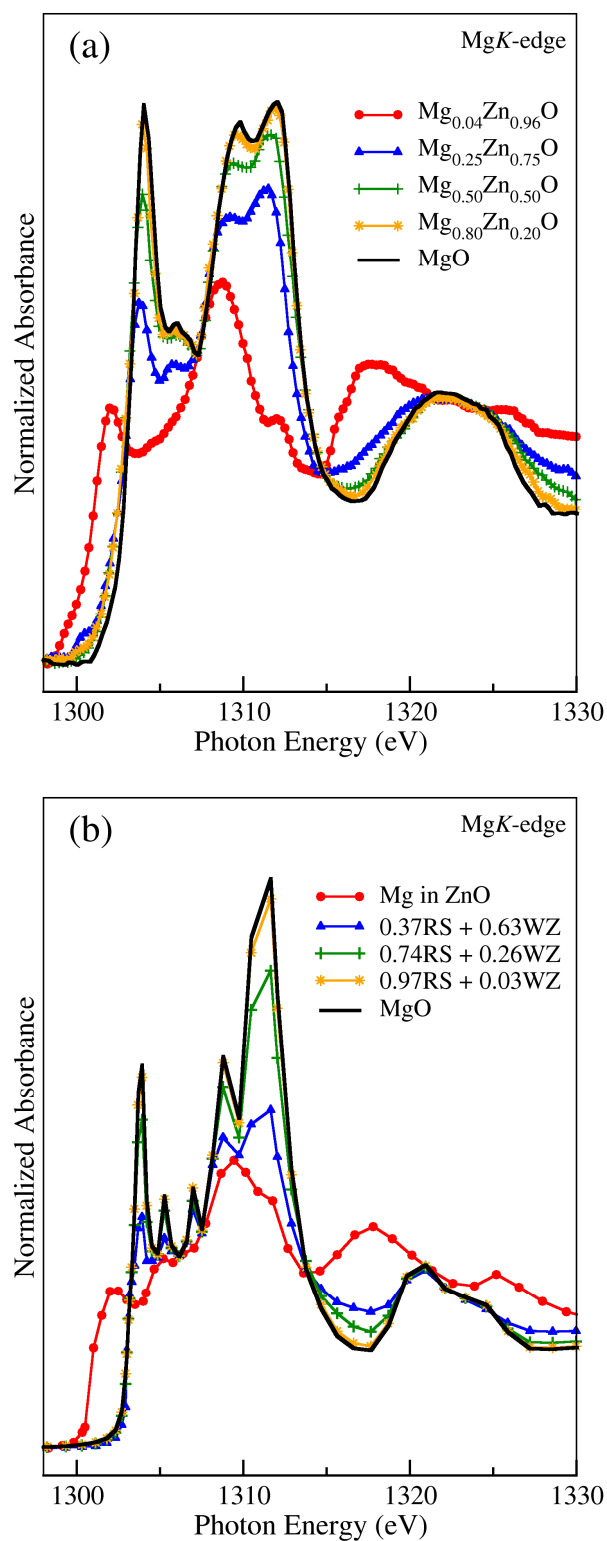
Figure 4.9 (a) The measured Mg K-edge XANES spectra of Mg$_x$Zn$_{1-x}$O nanocrystals, and (b) the calculated Mg K-edge XANES spectra from linear combination of MgO and Mg in ZnO with various proportions.

CHAPTER V

CONCLUSIONS

In this thesis, various compositions of $Mg_xZn_{1-x}O$ nanocrystals were prepared by a chemical method called oxalate-based co-precipitation. Standard characterization techniques such as XRD, EDS and TEM were used for microstructural studies of the synthesis nanocrystals.

It was found that the MZO nanocrystal samples with $x \leq 0.04$ exhibit pure WZ and the MZO samples with x $\geq$ 0.90 have RS structure. For $0.04 < x < 0.90$, the samples have mixed WZ and RS phases. There is no clear evidence for the composition that structural phase transition take place. The crystal grain size tended to decrease as the Mg content increased. The results agreed well with the measurements from transmission electron microscope and electron diffraction. From UV-VIS measurement, it clearly demonstrates that the bandgap of $Mg_xZn_{1-x}O$ nanocrystals increase as the Mg content increased.

Both Mg and Zn K-edges XANES spectra were utilized as a key characterization technique to probe the local structure around Mg and Zn atoms in MZO nanocrystals. By linear combination analysis the RS/WZ ratios were obtained for all MZO samples From RS/WZ, it was found that the majority of metal atoms occupy WZ sites for samples with low x and RS sites for samples with high x. Moreover, form XAS results, it can be concluded that for each sample (at the same concentration) Mg atom has higher RS/WZ ratio compared to that of Zn atom. This

can be viewed as the experimental evidence that in MZO alloys at thermal equilibrium, Mg atom prefers 6-fold site while Zn atom prefers 4-fold site. The RS/WZ ratios were also used for the simulation of XAS spectra using FEFF software. All features in the XANES spectra can be theoretical reproduced well in both Mg and Zn edges. The result is very useful for the local environment investigation of MZO nanostructure in the future nanoengineering.

REFERENCES

REFERENCES

Ankudinov, A. L., Ravel, B., Rehr, J. J., and Conradsan, S. D. (1998). Real-space multiple-scattering calculation and interpretation of x-ray-absorption near-edge structure. **Phys. Rev. B.** 58: 7565.

Brandon, D. G., and Kaplan, W. D. (1999). **Microstructural characterization of materials.** Chichester: Wiley.

Chen, N. B., and Sui, C. H. (2006). Recent progress in research on $Mg_xZn_{1-x}O$ alloys. **Mater. Sci. Eng. B** 126: 16. 128(6): 1853-1858.

Chiou, J. W., Tsai, H. M., Pao, C. W., Lee, J. F., and Guo, J. H. (2008). Mg-induced increase of band gap in $Zn_{1-x}Mg_xO$ nanorods revealed by x-ray absorption and emission spectroscopy. **J. Appl. Phys.** 104: 013709.

Choopun, S., Vispute, R. D., Yang, W., and Sharma, R. P. (2002). Realization of band gap above 5.0 eV in metastable cubic-phase $Mg_xZn_{1-x}O$ alloy films. **Appl. Phys. Lett.** 80: 1529.

Decremps, F., Datchi, F., Saitta, A. M., Polian. A., Pascarelli., Cicco, A. D., Itié, J. P., and Baudelet, F. (2003). Local structure of condensed zinc oxide. **Phys. Rev. B** 68: 104101.

Ertl, G., Knözinger, H., and Weitkamp, J. (1999). **Preparation of solid catalysts.** New York: Wiley.

Fong, C. Y., Weber, W., and Phillips, J. C. (1976). Violation of Vegard's law in covalent semiconductor alloys. **Phys. Rev. B** 14(2): 5387-5391.

Fultz, B., and Howe, J. M., (2008). **Transmission electron microscopy and diffractometry of materials** (3rd ed.). New York: Springer.

Guinier, A. (1994). **X-ray diffraction: In crystals, imperfect crystals, and amorphous bodies.** New York: W. H. Freeman.

Harvey, D. (2000). **Modern analytical chemistry.** New York: McGraw-Hill.

Kawai, J. (2000). **Absorpyion techniques in x-ray spectrometry, Encyclopedia of analytical chemistry.** New York: Wiley.

Kim, Y. and Hunt, W. D. (1994). Surface acoustic wave properties of ZnO films on {001}-cut<110>-propagating GaAs substrates. **J. Appl. Phys.** 75(1): 7299-7303.

Koningsberger, D. C. and Prins, R. (1998). **X-ray Absorption: Principles, Applications, Techniques of EXAFS, SEXAFS and XANES.** New York: Wiley.

Lee, J. H., Ko, K. K., and Park, B. O. (2003). Electrical and optical properties of ZnO transparent conducting films by the sol-gel method. **J. Crystal Growth.** 274: 119-125.

Lin, C. H., Chiou, B. S., Chang, C. H., and Lin, J. D. (2003). Preparation and cathodoluminescence of ZnO phosphor. **Mater. Chem. Phys.** 77: 647.

Lu, G., Lieberwirth, I., and Wegner, G. (2006). A General Polymer-based process to prepare mixed metal oxides: the case of Zn1-xMgxO nanoparticles. **J. Am. Chem. Soc.** 128: 15445-15450.

Maznichenko, I. V., Ernst, A., Bouhassoune, M., Henk, J., Däne, M., Lüders, M., Bruno, P., Hergert, W., Mertig, I., Szotek, Z., and Temmerman, W. M.

(2009). Structural phase transitions and fundamental band gap of $Mg_xZn_{1-x}O$ alloys from first principles. **Phys. Rev. B** 80:144101.

Narayan, J., Sharama, A. K., Kvit, A., Jin, C., Muth, J. F., and Holland, O. W. (2002). Novel cubic $Zn_xMg_{1-x}O$ epitaxial heterostructures on Si (100) substrates. **Solid State Commun.** 121: 9.

Norton, D. P., Pearton, S. J., Hebard, A. F., Thedoropoulou, N., Boatner, L. A., and Wilson, R. G. (2003). Ferromagnetism in Mn-implanted ZnO:Sn single crystals. **Appl. Phys. Lett.** 82: 239.

Ohtomo, A., Kawasaki, M., Koida, T., Masubuchi, K., Koinuma, H., Sakurai, Y., Yasuda, T., and Segawa, Y. (1998). $Mg_xZn_{1-x}O$ as a II–VI widegap semiconductor alloy. **Appl. Phys. Lett.** 72: 2466.

Ohtomo, A., Kawasaki, M., Sakurai, Y. and Ohkubo, I. (1998). Fabrication of alloys and superlattices based on ZnO towards ultraviolet laser. **Mater. Sci. Eng. B.** 56: 263.

Park, S. H., Kim, K. B., and Seo, S. Y. (2006). Structural and optical properties of $Zn_{1-x}Mg_xO$ thin films synthesized with metal organic chemical vapor deposition. **J. Electron Mater.** 35: 1680.

Park, W. I., Yi, G. C., and Jang, H. M. (2001). Metalorganic vapor-phase epitaxial growth and photoluminescent properties of $Zn_{1-x}Mg_xO$ ($0 < x < 0.49$) thin films. **Appl. Phys. Lett.** 79: 2022.

Qui, X., Li, L., Zheng, J., Liu, J., Sun, X., and Li, G. (2008). The enhanced photocatalytic activities of semiconductors, a case study of ZnO doped with Mg^{2+}. **J. Phys. Chem. C** 112: 12242-12248.

Rehr, J. J., and Albers, R. C. (2000). Theoretical approaches to x-ray absorption fine structure. **Rev. Mod. Phys.** 72: 621.

Rouessac, F., and Rouessac, A. (2004). **Chemical analysis: Modern instrumentation methods and techniques.** Chichester: Wiley.

Sarver, J. F., Katnack, F. L., and Hummel, F. A. (1959). Phase Equilibria and Manganese-Activated Fluorescence in the System $Zn_3(PO_4)_2$-$Mg_3(PO_4)_2$. **J. Electrochem. Soc.** 77: 647.

Sharma, A. K., Narayan, J., Muth, J. F., Teng, C. W., and Holland, O. W. (1999). Optical and structural properties of epitaxial $Mg_xZn_{1-x}O$ alloys. **Appl. Phys. Lett.** 75: 3327.

Wang, Z. L. (2004). Zinc oxide nanostructures: growth, properties and applications. **J. Phys. Conders. Matter.** 16: 829-858.

William, D. B., and Carter, C. B. **Transmission Electron Microscopy: A Textbook for Materials Science.** New York: Plenum Press.

Wong, E. M., and Searson, P. C. (1999). ZnO quantum particle thin films fabricated by electrophoretic deposition. **Appl. Phys. Lett.** 74(20): 2939-2941.

Yang, W., Hullavarad, S. S., Nagaraj, B., Takeuchi, I., Sharma, R. P., and Shen, H. (2003). Compositionally-tuned epitaxial cubic $Mg_xZn_{1-x}O$ on Si(100) for deep ultraviolet photodetectors. **Appl. Phys. Lett.** 82: 3424.

Young-II, K., Page, K. R., and Seshadri, R. (2007). Synchrotron x-ray study of polycrystalline wurtzite $Zn_{1-x}Mg_xO$ ($0 < x < 0.15$): Evolution of crystal structure and polarization. **Appl. Phys. Lett.** 90: 101904.

APPENDIX

Abstract submitted for the Siam Physics Congress 2010, Kanchanaburi (2010)

Local structure of $Mg_xZn_{1-x}O$ Nanocrystals

***J. Jutimoosik**[*], S. Limpijumnong and S. Rujirawat*

School of Physics, Institute of Science, Suranaree University of Technology,
and
Synchrontron Light Research Institute
Nakhon Ratchasima, Thailand.

Abstract

$Mg_xZn_{1-x}O$ (MZO) is an attractive material for deep ultraviolet optoelectronic device since the bandgap can be tuned over a broad range, from 3.3-7.8 eV. In this work, nanocrystalline MZO samples with x ranging from 0 to 1 were synthesized using an oxalate-based co-precipitation method. The samples were characterized by x-ray diffraction (XRD), energy dispersive x-ray spectroscopy (EDX), transmission electron microscopy (TEM), and x-ray absorption spectroscopy (XAS). From XRD measurements , the samples with x ≤ 0.1 exhibit pure wurtzite (WZ) structure and the samples with x ≥ 0.9 show rocksalt (RS) structure. The samples with concentration x between 0.1-0.9 have mixing of both WS and RS structures. No sharp structural transition regime was found. XAS indicated that Mg replace Zn in MZO WZ samples (low x). Additionally, Zn was found to be in the cation site in MZO RS sample (high x). However, the local structure around Zn was found to be distorted from the MgO RS structure. The finding is quite interesting when compared with the theoretical prediction of WZ to RS structural transition of MZO in the literature.

Keyword : $Mg_xZn_{1-x}O$, XRD, XAS

---

[*] Corresponding author. Email: jaru_tum@hotmail.com

Abstract submitted for the 19th International symposium on the Applications of Ferroelectrics, Edinburgh, Scotland (2010)

SYNCHROTRON X-RAY ABSORPTION STUDY OF Cu AND Mn DOPED BiFeO₃-BaTiO₃ MULTIFERROIC CERAMICS

S.Chandarak[1], J. Jutimoosik[2,3], S. Pojprapai[1], S.Srilomsak[1], S. Rujirawat[2,3], R.Yimnirun[3]

[1]School of Ceramic Engineering, Suranaree University of Technology, Nakhon Ratchasima 30000, Thailand

[2]Synchrotron Light Research Institute (Public Organization), Nakhon Ratchasima 30000, Thailand
[3]School of Physics, Institute of Science, Suranaree University of Technology, Nakhon Ratchasima 30000, Thailand
e-mail: rattikorn@sut.ac.th

In this work, an experimental X-ray Absorption Spectroscopy (XAS) measurement was employed to determine the local structure and valency of Cu and Mn in BiFeO₃-BaTiO₃. Synchrotron x-ray absorption near-edge structure (XANES) and extended x-ray absorption fine structure (EXAFS) experiments were performed on Cu-doped and Mn-doped BiFeO₃-BaTiO₃ samples. The Cu- and Mn-doped BiFeO₃-BaTiO₃ powder samples were used for the XAS experiment. XAS spectra at the Cu and Mn K-edge were recorded in flurorescent mode with 13-element Ge detector. The spectra were collected at ambient temperature with a Ge(111) double crystal monochromator and recorded after performing an energy calibration. The features of the measured Cu and Mn *K*-edge XANES and EXAFS were consistent with Cu and Mn on the Ti/Fe site and inconsistent with Cu and Mn on other sites. The clear agreement was the strongest evidence of Cu and Mn substituting for B-site in BiFeO₃-BaTiO₃ materials. In addition, the valency of both Cu and Mn ions in BiFeO₃-BaTiO₃ materials was also confirmed.

Submitting author's name:	Rattikorn Yimnirun
Institution:	Suranaree University of Technology
Address:	School of Physics, Institute of Science Suranaree University of Technology Nakhon Ratchasima 30000 Thailand
e-mail:	rattikorn@sut.ac.th *AND* rattikornyimnirun@yahoo.com
Topic identifier, from list on abstract page of ISAF-ECAPD 2010 website:	P. Characterization Techniques
Preferred mode of presentation (oral, poster, or either)	Poster
Proceedings to which you will submit your manuscript: ISAF or ECAPD	ECAPD

Abstract submitted for Pure and Applied Chemistry International Conference 2011, Bangkok (2011)

Probing Local Structure in Functional Oxide Materials with Synchrotron X-Ray Absorption Spectroscopy

Rattikorn Yimnirun [1]* Jaru Jutimoosik[1] Atipong Bootchanont[1] Sujittra Chandarak[2] Kanokwan Khanchiang[3,4] Teerawat Monnor[1,4] Muangjai Unruan[1] Yongyut Laosiritaworn[3,4] and Saroj Rujirawat[1,4,5]

[1] *School of Physics, Institute of Science, Suranaree University of Technology, Nakhon Ratchasima 30000, Thailand*
[2] *School of Ceramic Engineering, Institute of Engineering, Suranaree University of Technology, Nakhon Ratchasima 30000, Thailand*
[3] *Department of Physics and Materials Science, Faculty of Science, Chiang Mai University Chiang Mai 50200, Thailand*
[4] *ThEP Center, CHE, 328 Si Ayutthaya Road, Bangkok 10400, Thailand*
[5] *Synchrotron Light Research Institute (Public Organization), Nakhon Ratchasima 30000, Thailand*
E-mail: rattikorn@sut.ac.th

X-ray absorption spectroscopy (XAS) is proven to be a very powerful technique for resolving the local structure surrounding a particular (absorbing) atom. Traditionally, XAS is divided into two regions: (1) the low energy region, which covers photon energy up to about 40 eV above the absorption edge, called the x-ray absorption near-edge structure (XANES) and (2) the higher energy region from 40 eV up to ~1000 eV above the absorption edge, called the extended x-ray absorption fine structure (EXAFS). The XANES measurement can be used to determine the specific atom. In addition, the EXAFS measurement allows the identification of the nearest neighboring atoms to the absorbing atom to determine the coordination environment for the metal of interest. Recently, both techniques have been successfully applied to various classes of materials to obtain their local structures. In this work, we carried out a combined experimental investigation of the XAS measurement (both XANES and EXAFS regions) to determine the local structure of various functional oxide materials. The synchrotron XANES and EXAFS measurements were performed at the X-ray absorption spectroscopy beamline (BL-8) of the Synchrotron Light Research Institute (SLRI, Thailand). In this lecture, examples of how the XAS technique was employed in determining local structures of various functional oxide materials, such as $BaTiO_3$, $Pb(Zr,Ti)O_3$, and $BiFeO_3$, will be outlined and discussed.

CURRICULUM VITAE

Name   Mr. Jaru Jutimoosik

Date of Birth   21 July 1980

Place of Birth Nakhon Si Thamarat, Thailand

Nationality   Thai

Education

1999-2003   Kasetsart University, Bangkok, Thailand

                    Bachelor of Science (Physics)

2008-present   Currently enrolling in Master's degree majoring in Physics, School of Physics, Institute of Science, Suranaree University of Technology, Nakhon Ratchasima, Thailand